Published in *Journal of the Mechanics and Physics of Solids* (2022) **165**: 104925
doi: https://doi.org/10.1016/j.jmps.2022.104925

Interactions between multiple rigid lamellae in a ductile metal matrix: shear band magnification and attenuation in localization patterns

Diana Giarola[1], Francesco Dal Corso[1], Domenico Capuani[2], Davide Bigoni[1]*
[1] DICAM, University of Trento, via Mesiano 77, I-38123 Trento, Italy
[2] DA, University of Ferrara, via Quartieri 8, I-44121 Ferrara, Italy

August 8, 2022

Abstract

A ductile matrix material containing an arbitrary distribution of parallel and stiff lamellar ('rigid-line') inclusions is considered, subject to a prestress state provided by a simple shear aligned parallel to the inclusion lines. Because the lamellae have negligible thickness, the simple shear prestress state remains uniform and its amount can be high enough to drive the matrix material on the verge of ellipticity loss. Close to this critical stage, a uniform remote Mode I perturbation realizes shear band formation, growth, interaction, thickening or thinning. This two-dimensional problem is solved through the derivation of specific boundary integral equations, holding for a nonlinear elastic matrix material uniformly prestressed; the related numerical treatment is specifically tailored to capture the stress singularity present at the inclusion tips. Results show how complex localized deformation patterns form, so explaining features related to the failure mechanisms of ductile materials reinforced with stiff and thin inclusions. In particular, the influence of the inclusion distribution on the shear bands pattern is disclosed. Conditions for the magnification (the attenuation) of the localized deformations are revealed, fostering the progress (the setback) of the failure process.

1 Introduction

A distribution of hard inclusions enhances stiffness of a soft and ductile matrix, thus originating a material able to combine rigidity with toughness. This combination would not only realize the dream of medieval sword makers, but is highly requested in a number of advanced technical applications. For this reason, a great research effort has been directed to the development of metal matrix composites (MMC), where the matrix is a compliant metal, for instance, aluminum, magnesium, or titanium, while the reinforcement, in the form of particles, platelets, short or continuous fibres, may be another metal or a different, stiffer and stronger material, such as a ceramic (in which case the composite is called 'cermet' [46]). In this field, stiff lamellar inclusions are common and can be present as parallel distributions, as for instance in materials mimicking nacre [17]. Due to their high-contrast stiffness with the matrix and their high slenderness, the lamellae are also called 'rigid-line inclusions'.

Although beneficial for stiffness (and other properties such as hardness and resistance to decomposition by heat or chemical attack), the introduction of stiff lamellar inclusions plays a complex role on the effective strength. It has been proven both theoretically [3, 6, 11, 13, 21, 30, 32, 39] and experimentally [27, 28, 35, 37] that stiff lamellar inclusions create a strong stress concentration in the matrix material, which may lead to premature failure by shear band or crack nucleation and growth [47]. Therefore, the study of shear banding represents a key for the design of materials with superior mechanical properties.

The framework introduced by Dal Corso and Bigoni [12] is extended in the present article to the analysis of interactions between multiple rigid-line inclusions, all aligned parallel to a simple shear deformation of arbitrary amount, applied to an infinite matrix material. Under the assumed distribution of inclusions, the prestress state introduced through shearing remains uniform and can be increased up to the verge of ellipticity loss. A new boundary integral equation is obtained,

[1]Corresponding author: Davide Bigoni; web-site: http://bigoni.dicam.unitn.it; e-mail: bigoni@ing.unitn.it

Published in *Journal of the Mechanics and Physics of Solids* (2022) **165**: 104925
doi: https://doi.org/10.1016/j.jmps.2022.104925

governing the incremental response of a uniformly prestressed elastic material containing the rigid-line lamellae and subject to a remote perturbation, selected of Mode I in the applications. The integral equation allows for the numerical solution of problems involving several inclusions [16, 14, 24], so disclosing a series of important features related to interaction between shear bands and obstacles, involving nucleation, growth, thickening or thinning of the localized deformation.

Although boundary integral approaches are particularly indicated and in wide use for problems involving singularities [8, 18, 33, 36, 40], finite elements permit large simulations, involving distributions of hundreds of inclusions, which can be investigated during an evolutive strain path in a fully elasto-damaging material [22, 23]. From this point of view, finite elements appear to be superior to boundary integral techniques. However, the boundary integral technique proposed in the present article, even if based on the simplifying assumptions inherent to an incremental formulation, still presents a number of merits, leading to a highly refined definition of the mechanical fields under investigation. The merits are those typical of a boundary integral formulation and include: (i.) the discretization of only the boundaries of the lamellae and (ii.) a highly-precise representation of the singularity at the tips of the inclusions. In addition, and importantly for problems of material stability, (iii.) the integral approach permits the direct modelling of an infinite domain, so that the 'van Hove' conditions are enforced, ruling out all possible bifurcations occurring before loss of ellipticity and allowing for the shear bands emergence in a uniformly prestressed material [4].[1]

The mechanical problem of a distribution of parallel rigid-line inclusions embedded in an elastic matrix subject to simple shear is introduced (Section 2) and used to obtain the boundary integral equation governing the incremental response of the inclusion to a remote perturbation (Section 3). A numerical scheme is introduced (Section 4) to perform simulations and capable of resolving the complex mechanical fields developing during the blow-up of shear band patterns near several lamellae. Beside a validation of the proposed scheme with the analytical solution for one (obtained in [12]) and two collinear lamellae (Section 5.1), sets of two, four, and five lamellae are investigated with different lengths and arranged in different configurations within an incompressible matrix obeying J_2–deformation of plasticity (Sections 5.2 and 5.3).

The presented results demonstrate that the rigid lamellae distribution may be tuned to shield or to amplify the emergence of shear band networks, as the result of weakening or strengthening of the complex mechanical interactions between inclusions and localized strain. It is shown that shear band magnification is produced by the merging of two shear bands, whereas shear bands are cut down when intersecting a rigid lamella.

2 Rigid lamellae in an infinite medium

A distribution of N rigid-line (zero-thickness) inclusions, of half-length $l^{(n)}$ ($n = 1, ..., N$), is considered embedded within an infinite homogeneous elastic matrix (Fig. 1, left). In the undeformed state, each inclusion is parallel and orthogonal to the $\hat{X}_1$ and $\hat{X}_2$ axes respectively and has its center located at the point $\mathbf{C}^{(n)}$ ($n = 1, ..., N$), so that the n-th rigid inclusion occupies the line domain $\mathscr{R}^{(n)}$, defined as

$$\mathscr{R}^{(n)} := \left\{ \left| \hat{X}_1 - C_1^{(n)} \right| \leq l^{(n)}, \hat{X}_2 = C_2^{(n)} \right\}, \qquad n = 1, ..., N. \tag{1}$$

Application of a remote simple shear state parallel to the $\hat{X}_1$ axis (Fig. 1, right) realizes a uniform prestress state, because all the inclusions are parallel to the simple shear direction, which is a zero-elongation line. Therefore, the point

[1] The possibility of treating an infinite domain containing the rigid inclusions is made available through the use of the integral equation introduced here and is fundamental for problems of material instability. In fact, in an exact (consistently derived from a nonlinear formulation) incremental analysis of a homogeneously-strained material element, loss of ellipticity, corresponding to shear band formation, is the last of a series of subsequent instabilities, including, when possible, Euler-type, or bulging, or surface bifurcation (the latter being always possible when at least a part of the boundary is free from imposed displacements). After the first of these instabilities is encountered, homogeneity of the material element is lost. Therefore, it is impossible to reach the ultimate state for shear band formation in a homogeneous sample, except when the van Hove conditions are met, in which case, homogeneity of strain and stress is preserved up to failure of ellipticity. The van Hove conditions either correspond to displacements prescribed over the whole boundary of a sample or to an infinite domain. In the former case boundary displacements, while in the latter remote conditions, have to be consistent with uniform strain. Therefore, within a large strain formulation, enforcement of the van Hove conditions represents the only route to the analysis of strain localization into planar bands in a uniformly strained and stressed material element.

Published in *Journal of the Mechanics and Physics of Solids* (2022) **165**: 104925
doi: https://doi.org/10.1016/j.jmps.2022.104925

$\hat{\mathbf{X}} = \{\hat{X}_1, \hat{X}_2\}$ is transformed into the point $\hat{\mathbf{x}} = \{\hat{x}_1, \hat{x}_2\}$ as follows

$$\hat{x}_1 = \hat{X}_1 + \gamma\, \hat{X}_2, \qquad \text{and} \qquad \hat{x}_2 = \hat{X}_2, \tag{2}$$

where the dimensionless parameter γ rules the shear amount [4, 12], and consequently the line domain $\mathscr{R}^{(n)}$ is transformed into the line domain $\mathscr{r}^{(n)}$,

$$\mathscr{r}^{(n)} := \left\{ \left| \hat{x}_1 - C_1^{(n)} - \gamma C_2^{(n)} \right| \leq l^{(n)}, \hat{x}_2 = C_2^{(n)} \right\}, \qquad n = 1, ..., N. \tag{3}$$

Considering an initially isotropic elastic matrix, the principal Cauchy prestress components σ_1 and σ_2 are parallel to the principal prestretches λ_1 and λ_2,

$$\lambda_{1,2} = \pm\frac{\gamma}{2} + \sqrt{1 + \left(\frac{\gamma}{2}\right)^2}, \tag{4}$$

and are aligned parallel to the x_1 and x_2 axes and inclined at the Eulerian (anti-clockwise) angle θ_E, measured with respect to the $\hat{x}_1$ and $\hat{x}_2$ axes,

$$\theta_E = \frac{1}{2}\arctan\frac{2}{\gamma}. \tag{5}$$

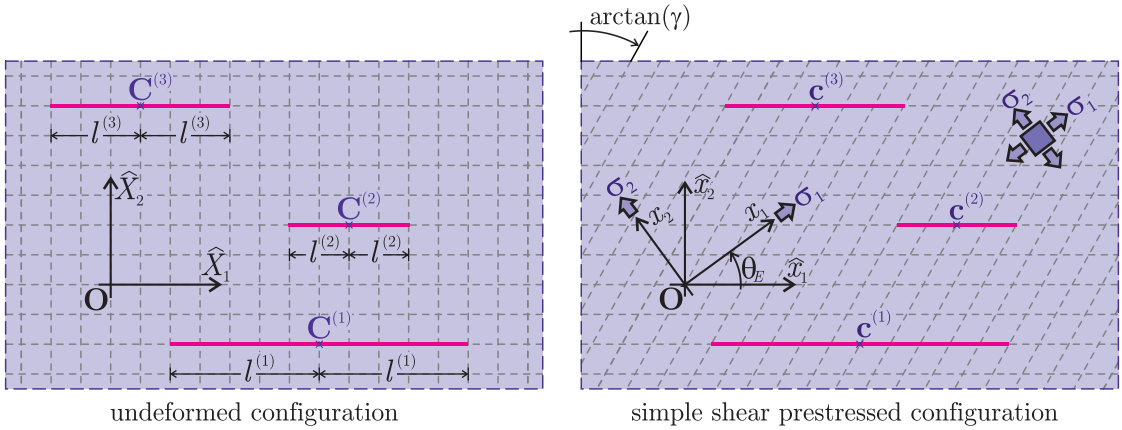

Figure 1: Distribution of N rigid-line inclusions of length $2l^{(n)}$ $(n = 1, ..., N)$ aligned parallel to the $\hat{x}_1$–axis. The reference, unstrained, configuration is shown on the left, while on the right the configuration is reported after the application of a simple shear deformation (of amount γ), parallel to the lamellae. A Mode I perturbation (not shown) is eventually applied on the strained configuration.

The incremental response of the prestressed elastic material is described by the following linear constitutive equation, relating the increment of the nominal stress (transpose of the first Piola-Kirchhoff stress), $\hat{t}_{ij}$ $(i, j = 1, 2)$, to the incremental displacement gradient, $\hat{v}_{l,k}$ $(l, k = 1, 2)$,

$$\hat{t}_{ij} = \begin{cases} \hat{\mathbb{K}}_{ijkl}\hat{v}_{l,k}, & \text{for compressible material,} \\ \hat{\mathbb{K}}_{ijkl}\hat{v}_{l,k} + \dot{p}\,\delta_{ij}, & \text{for incompressible material,} \end{cases} \tag{6}$$

where repeated indices are summed, the subscript k after a comma denotes differentiation with respect to the $\hat{x}_k$–axis, and $\hat{\mathbb{K}}_{ijkl}$ are the components of the fourth-order incremental constitutive tensor. In the case of incompressible material, a Lagrangian multiplier $\dot{p}$ enters the formulation, representing the incremental mean stress, multiplied by the Kronecker delta δ_{ij} and the following internal constraint on the incremental displacement is enforced,

$$\hat{v}_{i,i} = 0, \qquad \text{for incompressible material.} \tag{7}$$

Published in *Journal of the Mechanics and Physics of Solids* (2022) **165**: 104925
doi: https://doi.org/10.1016/j.jmps.2022.104925

At this stage, the material, uniformly prestressed under the shear amount γ, is perturbed through an incremental Mode I loading. More specifically, a linear incremental displacement is remotely applied under Mode I

$$\lim_{|\hat{\mathbf{x}}|\to\infty} \hat{v}_1(\hat{x}_1,\hat{x}_2) = \hat{v}^{\infty}_{1,1}\hat{x}_1, \qquad \lim_{|\hat{\mathbf{x}}|\to\infty} \hat{v}_2(\hat{x}_1,\hat{x}_2) = \hat{v}^{\infty}_{2,2}\hat{x}_2, \tag{8}$$

where $\hat{v}^{\infty}_{1,1}$ and $\hat{v}^{\infty}_{2,2}$ define the two normal incremental strains at infinity, which are independent variables when the material is compressible, but become constrained by $\hat{v}^{\infty}_{2,2} = -\hat{v}^{\infty}_{1,1}$ in the incompressible case, eqn (7). The presence of the rigid-line inclusions introduce further constraints on the perturbation of the mechanical fields. In particular, the incremental displacement field along each line inclusion is constrained to suffer an incremental rigid-body movement

$$\begin{aligned} &\hat{v}_1(\hat{x}_1,\hat{x}_2) = \eta^{(n)}_1, \\ &\hat{v}_2(\hat{x}_1,\hat{x}_2) = \eta^{(n)}_2 + \omega^{(n)}\left(\hat{x}_1 - C^{(n)}_1 - \gamma C^{(n)}_2\right), \end{aligned} \qquad \text{for } \hat{\mathbf{x}} \in \mathscr{r}^{(n)}, \qquad n = 1,...,N, \tag{9}$$

where $\eta^{(n)}_1$ and $\eta^{(n)}_2$ denote the incremental translation of the inclusion center in the $\hat{x}_1$–$\hat{x}_2$ coordinate system, while $\omega^{(n)}$ is the incremental rigid-body rotation of the inclusion.

Under quasi-static conditions, the incremental stress field $\hat{t}_{ij}$ obeys the incremental equilibrium equations

$$\hat{t}_{ij,i} = 0, \tag{10}$$

and generates tractions on each inclusion providing null values for the incremental resultant forces and moment, respectively,

$$\begin{aligned} &\int_{\mathscr{r}^{(n)}} [\![\hat{t}_{21}(\hat{x}_1,\hat{x}_2)]\!]\, \mathrm{d}\hat{x}_1 = 0, \\ &\int_{\mathscr{r}^{(n)}} [\![\hat{t}_{22}(\hat{x}_1,\hat{x}_2)]\!]\, \mathrm{d}\hat{x}_1 = 0, \\ &\int_{\mathscr{r}^{(n)}} \left(\hat{x}_1 - C^{(n)}_1 - \gamma C^{(n)}_2\right) [\![\hat{t}_{22}(\hat{x}_1,\hat{x}_2)]\!]\, \mathrm{d}\hat{x}_1 = 0, \end{aligned} \qquad \forall n = 1,...,N, \tag{11}$$

where the brackets $[\![\cdot]\!]$ denote the jump of the relevant quantity across the upper and lower face of the rigid-line inclusion,

$$[\![f\left(\hat{x}_1,\hat{x}_2\right)]\!] = \lim_{\epsilon\to 0}\left(f\left(\hat{x}_1,\hat{x}_2+|\epsilon|\right) - f\left(\hat{x}_1,\hat{x}_2-|\epsilon|\right)\right). \tag{12}$$

Finally, it is instrumental to recall that the incremental displacement $\mathbf{v}$, the nominal stress increment $\dot{\mathbf{t}}$, and the constitutive tensor $\mathbb{K}$ (expressed in the principal reference system $x_1 - x_2$) are related to the respective quantities ($\hat{\mathbf{v}}$, $\hat{\mathbf{t}}$, $\hat{\mathbb{K}}$) in the reference system $\hat{x}_1 - \hat{x}_2$ through the following rotation rules,

$$v_i = Q_{ij}\hat{v}_j, \quad \dot{t}_{ij} = Q_{il}Q_{jm}\hat{t}_{lm}, \quad \mathbb{K}_{ijhk} = Q_{il}Q_{jm}Q_{hn}Q_{ko}\hat{\mathbb{K}}_{lmno}, \tag{13}$$

where Q_{ij} are the components of the rotation tensor $\mathbf{Q}$

$$[\mathbf{Q}] = \begin{bmatrix} \cos\theta_E & \sin\theta_E \\ -\sin\theta_E & \cos\theta_E \end{bmatrix}. \tag{14}$$

Before moving to the boundary integral equations (presented in the next section), it is worth noting that a square root singularity may arise in the nominal stress field at the two tips of each rigid inclusion. Following the stress intensity factor normalization based on strain measures as in [11, 12, 13, 26, 27, 28, 37], the incremental Mode I stress intensity factors (SIFs) $\hat{K}^{(n)}_{I,L}$ at the left and $\hat{K}^{(n)}_{I,R}$ at the right tip of the n-th rigid inclusion are given by

$$\left.\begin{matrix} \hat{K}^{(n)}_{I,L} \\ \hat{K}^{(n)}_{I,R} \end{matrix}\right\} = \lim_{r\to 0^+} 2\mu\sqrt{\pi r}\,\hat{v}_{1,1}\left(C^{(n)}_1 + \gamma C^{(n)}_2 \mp \left(l^{(n)} + r\right), C^{(n)}_2\right), \tag{15}$$

Published in *Journal of the Mechanics and Physics of Solids* (2022) **165**: 104925
doi: https://doi.org/10.1016/j.jmps.2022.104925

where μ is the incremental shear modulus for a shear parallel to the x_1-axis, and the plus/minus sign is related to right/left tip. Finally, it is recalled that in the case of an isolated rigid-line inclusion (N=1, $l^{(1)} = l$) embedded in an unbounded matrix, uniformly prestressed and subject to a uniform remote incremental loading, the two tips display the same incremental stress intensification, $\hat{K}_{I,L}^{(1)} = \hat{K}_{I,R}^{(1)} = \hat{K}_I^{(N=1)}$, corresponding to

$$\hat{K}_I^{(N=1)} = 2\mu\, \hat{v}_{1,1}^{\infty} \sqrt{\pi l}. \tag{16}$$

3 Integral equation formulation

The incremental displacement $\hat{v}_g$ at the point $\hat{\mathbf{y}}$ of a prestressed hyperelastic solid can be evaluated through the following integral equation [5, 34, 38]

$$\hat{v}_g(\hat{\mathbf{y}}) = \int_{\partial\mathscr{B}} \left(\hat{t}_{ij}(\hat{\mathbf{x}})\hat{n}_i(\hat{\mathbf{x}})\hat{v}_j^g(\hat{\mathbf{x}}-\hat{\mathbf{y}}) - \hat{t}_{ij}^g(\hat{\mathbf{x}}-\hat{\mathbf{y}})\hat{n}_i(\hat{\mathbf{x}})\hat{v}_j(\hat{\mathbf{x}}) \right) \mathrm{d}l_{\hat{\mathbf{x}}}, \tag{17}$$

valid for a simply connected body $\mathscr{B}$, subject to mixed conditions on its boundary $\partial\mathscr{B}$ of unit outward normal $\hat{\mathbf{n}}$. In equation (17), the tensor $\hat{t}_{ij}$ is the incremental nominal stress produced by the incremental displacement field $\hat{v}_j$ while $\hat{t}_{ij}^g$ is the incremental nominal stress related to the infinite body displacement Green function $\hat{v}_j^g$ [5]

$$\hat{v}_j^g(\hat{\mathbf{x}}) = -\frac{1}{4\pi^2} \oint_{|\mathbf{m}|=1} \hat{A}_{jg}^{-1}(\mathbf{m}) \, \log|\mathbf{m}\cdot\hat{\mathbf{x}}| \mathrm{d}s_{\mathbf{m}}, \tag{18}$$

in which $\hat{A}_{jg}(\mathbf{m})$ is the acoustic tensor pertaining to the elastic body under consideration and $\mathbf{m}$ is a unit vector,

$$\hat{A}_{jg}(\mathbf{m}) = m_k \hat{\mathbb{K}}_{kjhg} m_h. \tag{19}$$

When an infinite body is subject to a remote linearly-varying displacement $\hat{v}_g^{\infty}$ and contains N inclusions of domain $\mathcal{S}^{(n)}$, the incremental displacement $\hat{v}_g$ at any point $\hat{\mathbf{y}}$ inside the medium, can be obtained from equation (17), where the boundary of the integral is reduced to the inclusion interfaces $\partial\mathcal{S}^{(n)}$ $(n = 1, ..., N)$

$$\hat{v}_g(\hat{\mathbf{y}}) = \hat{v}_g^{\infty}(\hat{\mathbf{y}}) + \sum_{n=1}^{N} \int_{\partial\mathcal{S}^{(n)}} \left(\hat{t}_{ij}(\hat{\mathbf{x}})\hat{n}_i(\hat{\mathbf{x}})\hat{v}_j^g(\hat{\mathbf{x}}-\hat{\mathbf{y}}) - \hat{t}_{ij}^g(\hat{\mathbf{x}}-\hat{\mathbf{y}})\hat{n}_i(\hat{\mathbf{x}})\hat{v}_j(\hat{\mathbf{x}}) \right) \mathrm{d}l_{\hat{\mathbf{x}}}, \tag{20}$$

where $\hat{\mathbf{n}}$ is the unit normal at the matrix-inclusion interface, outward to the matrix and therefore inward to the inclusion. Equation (20) is valid for any (compressible or incompressible) elastic material, uniformly prestressed [7, **?**].

Considering that each inclusion has the shape of a zero-thickness line located as described in the previous section, the inclusion interface $\partial\mathcal{S}^{(n)}$ reduces to

$$\partial\mathcal{S}^{(n)} = \mathscr{r}^{(n)+} \cup \mathscr{r}^{(n)-}, \qquad n = 1, ..., N, \tag{21}$$

where $\mathscr{r}^{(n)+}$ and $\mathscr{r}^{(n)-}$ are the two major sides of the n-th inclusion of length $l^{(n)}$ and assumed of vanishing thickness 2ϵ

$$\mathscr{r}^{(n)\pm} := \left\{ \left| \hat{x}_1 - C_1^{(n)} - \gamma C_2^{(n)} \right| \le l^{(n)}, \hat{x}_2 = C_2^{(n)} \pm |\epsilon| \right\}, \qquad n = 1, ..., N, \tag{22}$$

with corresponding unit normal $\hat{\mathbf{n}}$ defined as

$$\hat{\mathbf{n}}|_{\mathscr{r}^{(n)+}} = -\,\hat{\mathbf{n}}|_{\mathscr{r}^{(n)-}}, \qquad \text{with} \qquad \hat{n}_1\big|_{\mathscr{r}^{(n)-}} = 0, \qquad \hat{n}_2\big|_{\mathscr{r}^{(n)-}} = 1. \tag{23}$$

In the limit of vanishing inclusion thickness, $\epsilon \to 0$, and considering the definition of the line domain $\mathscr{r}^{(n)}$, equation (3), of the unit normal $\hat{\mathbf{n}}$, equation (23), and of the jump operator, equation (12), the integral equation (20) simplifies to

$$\hat{v}_g(\hat{\mathbf{y}}) = \hat{v}_g^{\infty}(\hat{\mathbf{y}}) - \sum_{n=1}^{N} \int_{\mathscr{r}^{(n)}} \left([\![\hat{t}_{2j}(\hat{\mathbf{x}})]\!] \, \hat{v}_j^g(\hat{\mathbf{x}}-\hat{\mathbf{y}}) - \hat{t}_{2j}^g(\hat{\mathbf{x}}-\hat{\mathbf{y}}) \, [\![\hat{v}_j(\hat{\mathbf{x}})]\!] \right) \mathrm{d}\hat{x}_1. \tag{24}$$

Recalling that across a rigid-line inclusion the displacement field is continuous,

$$[\![\hat{\mathbf{v}}(\hat{\mathbf{x}})]\!] = \mathbf{0}, \qquad \text{for } \hat{\mathbf{x}} \in \mathscr{r}^{(n)}, \qquad n = 1, ..., N, \tag{25}$$

equation (24) finally reduces to

$$\hat{v}_g(\hat{\mathbf{y}}) = \hat{v}_g^{\infty}(\hat{\mathbf{y}}) - \sum_{n=1}^{N} \int_{\mathscr{r}^{(n)}} [\![\hat{t}_{2j}(\hat{\mathbf{x}})]\!]\, \hat{v}_j^g(\hat{\mathbf{x}} - \hat{\mathbf{y}}) \mathrm{d}\hat{x}_1, \tag{26}$$

representing the boundary integral equation valid for an infinite medium, uniformly prestressed, containing N rigid-line inclusions, incrementally loaded through remote incremental linear displacement $\hat{v}_g^{\infty}$.

According to the rotation rule for second-order tensors, equation $(13)_2$, the transformation between the displacement Green functions, $\hat{\mathbf{v}}^g$ in the $\hat{x}_1 - \hat{x}_2$ reference system and $\mathbf{v}^g$ in the $x_1 - x_2$ reference system, is given by

$$\hat{v}_j^g = Q_{lj} Q_{kg} v_l^k, \tag{27}$$

so that the boundary integral equation (26) can be rewritten as

$$\hat{v}_g(\hat{\mathbf{y}}) = \hat{v}_g^{\infty}(\hat{\mathbf{y}}) - Q_{lj} Q_{kg} \sum_{n=1}^{N} \int_{\mathscr{r}^{(n)}} [\![\hat{t}_{2j}(\hat{\mathbf{x}})]\!]\, v_l^k \left(\mathbf{Q}^T(\hat{\mathbf{x}} - \hat{\mathbf{y}})\right) \mathrm{d}\hat{x}_1, \tag{28}$$

where the superscript T denotes the transpose operator.

The jump in the nominal stress $[\![\hat{t}_{2j}(\hat{\mathbf{x}})]\!]$ across the N rigid-line inclusions and the $3N$ rigid-body displacements ($\eta_1^{(n)}$, $\eta_2^{(n)}$, and $\omega^{(n)}$) are unknown at this stage. These quantities can be obtained by substituting the integral equation (28) into the $3N$ equations of incremental equilibrium of each rigid-line inclusion, eqns (11), and into the incremental rigid-body movement constraint (9), which can be rewritten as

$$\begin{aligned}
\hat{v}_1^{\infty}(\hat{\mathbf{y}}) - Q_{lj} Q_{k1} \sum_{n=1}^{N} \int_{\mathscr{r}^{(n)}} [\![\hat{t}_{2j}(\hat{\mathbf{x}})]\!]\, v_l^k \left(\mathbf{Q}^T(\hat{\mathbf{x}} - \hat{\mathbf{y}})\right) \mathrm{d}\hat{x}_1 &= \eta_1^{(m)}, \\
\hat{v}_2^{\infty}(\hat{\mathbf{y}}) - Q_{lj} Q_{k2} \sum_{n=1}^{N} \int_{\mathscr{r}^{(n)}} [\![\hat{t}_{2j}(\hat{\mathbf{x}})]\!]\, v_l^k \left(\mathbf{Q}^T(\hat{\mathbf{x}} - \hat{\mathbf{y}})\right) \mathrm{d}\hat{x}_1 &= \eta_2^{(m)} + \omega^{(m)} \left(\hat{y}_1 - C_1^{(m)} - \gamma C_2^{(m)}\right),
\end{aligned} \tag{29}$$

for $\hat{\mathbf{x}} \in \mathscr{r}^{(n)}$ and $\hat{\mathbf{y}} \in \mathscr{r}^{(m)}$ with $\{n, m\} = 1, ..., N$.

Finally, towards the evaluation of the incremental Mode I stress intensity factor, equation (15), a differentiation of equation (26) in the $\hat{x}_1 - \hat{x}_2$ reference system provides the gradient of incremental displacement

$$\hat{v}_{g,i}(\hat{\mathbf{y}}) = \hat{v}_{g,i}^{\infty}(\hat{\mathbf{y}}) - \sum_{n=1}^{N} \int_{\mathscr{r}^{(n)}} [\![\hat{t}_{2j}(\hat{\mathbf{x}})]\!]\, \hat{v}_{j,i}^g (\hat{\mathbf{x}} - \hat{\mathbf{y}})\, \mathrm{d}\hat{x}_1. \tag{30}$$

According to the rotation rules, equation (13), the transformation involving the Green functions for gradient of the displacement is

$$\hat{v}_{j,i}^g = Q_{mi} Q_{lj} Q_{kg} v_{l,m}^k, \tag{31}$$

where the subscript m after a comma applied to the Green function $\mathbf{v}^k$ denotes differentiation with respect to the x_m–axis, so that the boundary integral equation (30) can be rewritten as

$$\hat{v}_{g,i}(\hat{\mathbf{y}}) = \hat{v}_{g,i}^{\infty}(\hat{\mathbf{y}}) - Q_{mi} Q_{lj} Q_{kg} \sum_{n=1}^{N} \int_{\mathscr{r}^{(n)}} [\![\hat{t}_{2j}(\hat{\mathbf{x}})]\!]\, v_{l,m}^k \left(\mathbf{Q}^T(\hat{\mathbf{x}} - \hat{\mathbf{y}})\right) \mathrm{d}\hat{x}_1. \tag{32}$$

Therefore, the incremental SIFs $\hat{K}_I$ under Mode I, equation (15), are given by

$$\left.\begin{matrix} \hat{K}_{I,L}^{(n)} \\ \hat{K}_{I,R}^{(n)} \end{matrix}\right\} = -2\mu Q_{q1} Q_{lj} Q_{k1} \lim_{r \to 0^+} \sqrt{\pi r} \sum_{m=1}^{N} \int_{\mathscr{r}^{(m)}} [\![\hat{t}_{2j}(\hat{\mathbf{x}})]\!]\, v_{l,q}^k \left(\mathbf{Q}^T \left(\hat{x}_1 - C_1^{(n)} - \gamma C_2^{(n)} \mp \left(l^{(n)} + r\right), C_2^{(m)} - C_2^{(n)}\right)\right) \mathrm{d}\hat{x}_1. \tag{33}$$

Published in *Journal of the Mechanics and Physics of Solids* (2022) **165**: 104925
doi: https://doi.org/10.1016/j.jmps.2022.104925

4 Numerical treatment of the boundary integral equation

The collocation method is exploited to numerically solve the integral equations for the incremental equilibrium (11) and rigid-body displacement (29) of the inclusion. A special technique has to be applied to treat the stress singularity at the inclusion tips [19, 20]. In particular, the mixed boundary element method [10, 19, 31] is implemented here with the use of discontinuous elements [9, 42], necessary to overcome the difficulty connected with the singularity of the traction occurring at corner points, which correspond to the lamellae tips in our case [15, 29].

Before considering a specific collocation node positioning, the discretization for the lamellae and the related stress jumps is introduced in general terms (Fig. 2). The n-th lamella is subdivided into $E^{(n)}$ elements, each of length $\Delta_e^{(n)}$ ($e = 1, ..., E^{(n)}$), therefore

$$\sum_{e=1}^{E^{(n)}} \Delta_e^{(n)} = 2l^{(n)}, \qquad n = 1, ..., N, \tag{34}$$

where the e-th element of n-th line inclusion is defined by the following coordinate subset (in the deformed state)

$$\text{element } e \text{ of inclusion } n: \qquad \hat{x}_1 \in \left[\hat{x}_1^{(n)(e)},\ \hat{x}_1^{(n)(e)} + \Delta_e^{(n)}\right], \qquad \hat{x}_2 = C_2^{(n)}, \tag{35}$$

where

$$\hat{x}_1^{(n)(1)} = C_1^{(n)} + \gamma C_2^{(n)} - l^{(n)}, \qquad \hat{x}_1^{(n)(e)} = \hat{x}_1^{(n)(e-1)} + \Delta_{e-1}^{(n)}, \qquad e = 2, ..., E^{(n)}. \tag{36}$$

Each element e of the n-th inclusion is characterised by three nodes, with the j-th one characterized by the coordinate

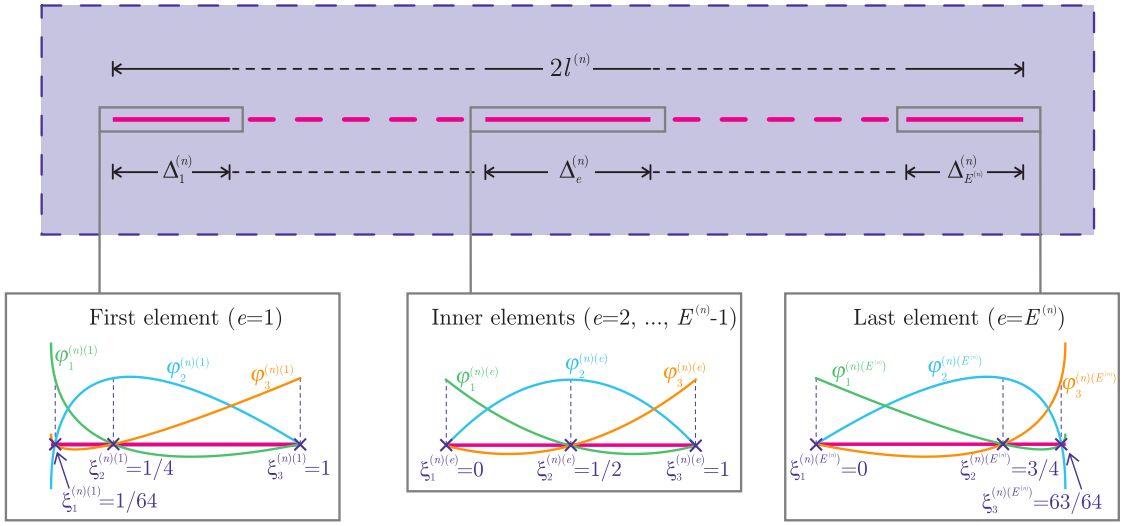

Figure 2: Discretization of the n-th lamella in $E^{(n)}$ elements (upper part) with the specification of collocation points and shape functions (lower part). Elements are continuous quadratic except at the two tips, where semi-discontinuous elements are adopted to capture the square-root singularity of the incremental stress.

$$\hat{x}_1^{(n)(e)(j)} = \hat{x}_1^{(n)(e)} + \xi_j^{(n)(e)} \Delta_e^{(n)}, \qquad j = 1, ..., 3, \tag{37}$$

where $\xi_j^{(n)(e)} \in [0, 1]$ is the dimensionless coordinate of the j-th node. By introducing the nodal value of stress jump $[\![\hat{t}_{2i}]\!]^{(n)(e)(j)}$ at the j-th node of the element number e inside the n-th rigid-line inclusion and the three respective shape functions $\varphi_j^{(n)(e)}(\xi)$, the stress jump field $[\![\hat{t}_{2i}]\!]$ along the n-th inclusion is approximated by

$$\left[\!\left[\hat{t}_{2i}\left(\hat{x}_1^{(n)(e)} + \xi\Delta_e^{(n)}, C_2^{(n)}\right)\right]\!\right] = \sum_{j=1}^{3} [\![\hat{t}_{2i}]\!]^{(n)(e)(j)} \varphi_j^{(n)(e)}(\xi), \qquad \xi \in [0, 1], \qquad i = 1, 2. \tag{38}$$

By means of representation (38), the incremental equations of rigid-body motion (29) are discretized at the q-th node of the f-th element along the m-th inclusion ($q = 1, 2, 3$; $f = 1, ..., E^{(m)}$; $m = 1, ..., N$) as

$$\begin{aligned}
&\hat{v}^{\infty}_{1,1}\,\hat{x}_1^{(m)(f)(q)} - Q_{kh}Q_{g1}\sum_{n=1}^{N}\sum_{e=1}^{E^{(n)}}\Delta_e^{(n)}\sum_{j=1}^{3}\left[\!\left[\hat{t}_{2h}\right]\!\right]^{(n)(e)(j)}\times\\
&\quad\times\int_0^1\varphi_j^{(n)(e)}(\xi)\;v_k^g\left(\mathbf{Q}^T\left(\hat{x}_1^{(n)(e)}+\xi\Delta_e^{(n)}-\hat{x}_1^{(m)(f)(q)},C_2^{(n)}-C_2^{(m)}\right)\right)\mathrm{d}\xi=\eta_1^{(m)},\\
&\hat{v}^{\infty}_{2,2}\,C_2^{(m)} - Q_{kh}Q_{g2}\sum_{n=1}^{N}\sum_{e=1}^{E^{(n)}}\Delta_e^{(n)}\sum_{j=1}^{3}\left[\!\left[\hat{t}_{2h}\right]\!\right]^{(n)(e)(j)}\times\\
&\quad\times\int_0^1\varphi_j^{(n)(e)}(\xi)v_k^g\left(\mathbf{Q}^T\left(\hat{x}_1^{(n)(e)}+\xi\Delta_e^{(n)}-\hat{x}_1^{(m)(f)(q)},C_2^{(n)}-C_2^{(m)}\right)\right)\mathrm{d}\xi=\eta_2^{(m)}+\omega^{(m)}\left(\hat{x}_1^{(m)(f)(q)}-C_1^{(m)}-\gamma C_2^{(m)}\right),
\end{aligned}\tag{39}$$

and the equations of incremental equilibrium (11) for the n-th inclusion ($n = 1, ..., N$) as

$$\begin{aligned}
&\sum_{e=1}^{E^{(n)}}\Delta_e^{(n)}\sum_{j=1}^{3}\left[\!\left[\hat{t}_{21}\right]\!\right]^{(n)(e)(j)}\int_0^1\varphi_j^{(n)(e)}(\xi)\mathrm{d}\xi=0,\\
&\sum_{e=1}^{E^{(n)}}\Delta_e^{(n)}\sum_{j=1}^{3}\left[\!\left[\hat{t}_{22}\right]\!\right]^{(n)(e)(j)}\int_0^1\varphi_j^{(n)(e)}(\xi)\mathrm{d}\xi=0,\\
&\sum_{e=1}^{E^{(n)}}\Delta_e^{(n)}\sum_{j=1}^{3}\left[\!\left[\hat{t}_{22}\right]\!\right]^{(n)(e)(j)}\int_0^1\left(\hat{x}_1^{(n)(e)}+\xi\Delta_e^{(n)}-C_1^{(n)}-\gamma C_2^{(n)}\right)\varphi_j^{(n)(e)}(\xi)\mathrm{d}\xi=0.
\end{aligned}\tag{40}$$

Equations (39) and (40) represent a linear system (whose explicit expression is reported in Appendix A) to be solved for the unknown values of nodal stress jumps ($\left[\!\left[\hat{t}_{21}\right]\!\right]^{(n)(e)(j)}$ and $\left[\!\left[\hat{t}_{22}\right]\!\right]^{(n)(e)(j)}$) and of rigid-body parameters ($\eta_1^{(n)}$, $\eta_2^{(n)}$, and $\omega^{(n)}$).

Once the nodal values of the stress jumps $\left[\!\left[\hat{t}_{21}\right]\!\right]^{(n)(e)(j)}$ are evaluated, the incremental mechanical fields are numerically obtained and the incremental SIFs at the two tips of the n-th inclusion can be assessed via eqns (33) through the following expression

$$\begin{aligned}
\left.\begin{matrix}\hat{K}_{I,L}^{(n)}\\ \hat{K}_{I,R}^{(n)}\end{matrix}\right\} = \;&-2\mu Q_{q1}Q_{lh}Q_{k1}\lim_{r\to0^+}\sqrt{\pi r}\sum_{m=1}^{N}\sum_{e=1}^{E^{(m)}}\sum_{j=1}^{3}\Delta_e^{(m)}\left[\!\left[\hat{t}_{2h}\right]\!\right]^{(m)(e)(j)}\times\\
&\times\int_0^1\varphi_j^{(m)(e)}(\xi)v_{l,q}^k\left(\mathbf{Q}^T\left(\hat{x}_1^{(m)(e)}-C_1^{(n)}-\gamma C_2^{(n)}\mp(l^{(n)}+r),C_2^{(m)}-C_2^{(n)}\right)\right)\mathrm{d}\xi.
\end{aligned}\tag{41}$$

From the practical point of view, the collocation nodes are considered to be located in such a way that two adjacent elements share their terminal node, so that the last node of every element coincides with the first node of the subsequent element,

$$\hat{x}_1^{(n)(e+1)(1)}=\hat{x}_1^{(n)(e)(3)},\qquad e=1,...,E^{(n)}-1,\qquad n=1,...,N,\tag{42}$$

and the discretization is symmetric along each line inclusion

$$\Delta_e^{(n)}=\Delta_{E^{(n)}-e+1}^{(n)},\qquad e=1,...,E^{(n)}.\tag{43}$$

More specifically, the considered discretization involves continuous quadratic elements along the whole line inclusion except at the two tip elements ($e = 1$ and $e = E^{(n)}$), where semi-discontinuous elements have been used. Considering that the quadratic shape functions $\varphi_j(\zeta)$ for a master element are

$$\varphi_1(\zeta)=\frac{(\zeta-\zeta_2)(\zeta-\zeta_3)}{(\zeta_1-\zeta_2)(\zeta_1-\zeta_3)},\qquad \varphi_2(\zeta)=\frac{(\zeta-\zeta_1)(\zeta-\zeta_3)}{(\zeta_2-\zeta_1)(\zeta_2-\zeta_3)},\qquad \varphi_3(\zeta)=\frac{(\zeta-\zeta_1)(\zeta-\zeta_2)}{(\zeta_3-\zeta_1)(\zeta_3-\zeta_2)},\tag{44}$$

where $\zeta \in [-1,1]$ is the master element coordinate and ζ_j $(j = 1,2,3)$ are the collocation points, by assuming the collocation points located at $\zeta_1 = -1$, $\zeta_2 = 0$, $\zeta_3 = 1$ and through the change of variable $\zeta = 2\xi - 1 \in [0,1]$, the collocation points and the shape functions for the continuous quadratic elements in the inner part of the lamella follow as

$$\begin{aligned} &\xi_1^{(n)(e)} = 0, && \varphi_1^{(n)(e)}(\xi) = 1 - 3\,\xi + 2\,\xi^2, \\ &\xi_2^{(n)(e)} = \frac{1}{2}, && \varphi_2^{(n)(e)}(\xi) = 4\,\xi - 4\,\xi^2, && e = 2, ..., E^{(n)} - 1. \\ &\xi_3^{(n)(e)} = 1, && \varphi_3^{(n)(e)}(\xi) = 2\,\xi^2 - \xi, \end{aligned} \tag{45}$$

Differently, in order to capture the singularity at the inclusion tips, specific quarter point semi-discontinuous elements are considered for the two tip elements ($e = 1$ and $e = E^{(n)}$) of each inclusion in order to properly display the square-root stress at the tips [9, 18, 45]. For the first element ($e = 1$), by assuming the collocation points located at $\zeta_1 = -3/4$, $\zeta_2 = 0$, $\zeta_3 = 1$ and through the (nonlinear) change of variable $\zeta = 2\sqrt{\xi} - 1$, the collocation points and the shape functions are

$$\begin{aligned} &\xi_1^{(n)(1)} = \frac{1}{64}, && \varphi_1^{(n)(1)}(\xi) = \frac{32}{21}\left(1 - 3\sqrt{\xi} + 2\xi\right), \\ &\xi_2^{(n)(1)} = \frac{1}{4}, && \varphi_2^{(n)(1)}(\xi) = -\frac{2}{3}\left(1 - 9\sqrt{\xi} + 8\xi\right), \\ &\xi_3^{(n)(1)} = 1, && \varphi_3^{(n)(1)}(\xi) = \frac{1}{7}\left(1 - 10\sqrt{\xi} + 16\xi\right), \end{aligned} \tag{46}$$

and, because of symmetry, for the last element ($e = E^{(n)}$) are

$$\xi_j^{(n)\left(E^{(n)}\right)} = 1 - \xi_{4-j}^{(n)(1)}, \qquad \varphi_j^{(n)\left(E^{(n)}\right)}(\xi) = \varphi_{4-j}^{(n)(1)}(1-\xi), \qquad j = 1,2,3. \tag{47}$$

In all of the numerical evaluations presented in the next section, each rigid-line inclusion is discretized adopting a minimum number of elements $E^{(n)} = 45$, through the following symmetric scheme. Two identical refined uniform meshes, with a minimum number of 20 elements each, are adopted near each tip for a length $l^{(n)}/5$. A coarse uniform mesh, with a minimum number of 5 elements, is used in the central part of the inclusion (of remaining length $8l^{(n)}/5$).

For the numerical computation of the incremental SIFs, a distance $r = 10^{-3}\, l^{(n)}$ from the inclusion tips, found to be sufficient for accurate estimation, has been considered.

5 Application to ductile metals: the J_2–deformation theory of plasticity

Incompressibility. Adopting incompressibility, the fourth-order elasticity tensor $\mathbb{K}_{ijkl}$ (which satisfies the major symmetry $\mathbb{K}_{ijkl} = \mathbb{K}_{klij}$) assumes under broad hypotheses the form [4]

$$\begin{aligned} &\mathbb{K}_{1111} = \mu_* - \frac{\sigma}{2} - \Pi, && \mathbb{K}_{1122} = -\mu_*, && \mathbb{K}_{1112} = \mathbb{K}_{1121} = 0, \\ &\mathbb{K}_{2211} = -\mu_*, && \mathbb{K}_{2222} = \mu_* + \frac{\sigma}{2} - \Pi, && \mathbb{K}_{2212} = \mathbb{K}_{2221} = 0, \\ &\mathbb{K}_{1212} = \mu + \frac{\sigma}{2}, && \mathbb{K}_{1221} = \mathbb{K}_{2112} = \mu - \Pi, && \mathbb{K}_{2121} = \mu - \frac{\sigma}{2}, \end{aligned} \tag{48}$$

where μ and μ_* are incremental shear moduli depending on the state of prestress through the in-plane deviatoric stress σ, and the mean stress Π defined as

$$\sigma = \sigma_1 - \sigma_2, \qquad \Pi = \frac{\sigma_1 + \sigma_2}{2}, \tag{49}$$

being σ_1 and σ_2 the two principal values of the Cauchy prestress. In the present case, the latter is generated by a simple shear, aligned parallel to the $x_1 - x_2$ reference system, which in turn is inclined at the angle θ_E with respect to the $\hat{x}_1 - \hat{x}_2$ reference system (where $\hat{x}_1$ is parallel to the inclusion line).

Due to incompressibility, the uniform Mode I loading applied at infinity, eqn (8), is subject to the constraint

$$\hat{v}^{\infty}_{2,2} = -\hat{v}^{\infty}_{1,1}. \tag{50}$$

The incremental Green's function v^k_l has been obtained by Bigoni and Capuani [5] for incompressible materials under plane strain conditions and is not repeated here for conciseness.

It is also interesting to note that the mean stress Π remains unprescribed in the following because, from the equation (48), it affects only the relation between incremental stress and incremental displacement gradient. Indeed, the unknowns of the boundary integral formulation are the incremental stress jumps $[\![\hat{t}_{21}]\!]$ and $[\![\hat{t}_{22}]\!]$ from which the incremental displacement components $\hat{v}_1$ and $\hat{v}_2$ can be evaluated through equation (26).

J_2–deformation theory of plasticity. Henceforth, the interactions between shear bands and rigid-line inclusions is analyzed by restricting the attention to a matrix material obeying the J_2–deformation theory of plasticity [25], whose nonlinear constitutive equations, when plane strain prevails, reduce to

$$\sigma_1 - \sigma_2 = \kappa \left(\frac{2}{\sqrt{3}}\right)^{H+1} \left|\ln \lambda_1\right|^{H-1} \ln \lambda_1, \tag{51}$$

where κ is a stiffness parameter, $H \in (0, 1]$ is the hardening exponent, while λ_1 is the principal stretch along the x_1-axis, related to the shear prestrain γ through equation (4).

Under the assumptions of plane strain and incompressibility, the incremental moduli μ and μ_* for the J_2-deformation theory material can be obtained as [4]

$$\mu = \frac{\kappa}{2}\left(\frac{2}{\sqrt{3}}\right)^{H+1} \left|\ln \lambda_1\right|^{H-1} \ln \lambda_1 \coth\left(2 \ln \lambda_1\right), \qquad \mu_* = H\,\frac{\kappa}{4}\left(\frac{2}{\sqrt{3}}\right)^{H+1} \left|\ln \lambda_1\right|^{H-1}. \tag{52}$$

For the non-linear elastic material (51), failure of ellipticity and shear band formation is determined as the solution of the nonlinear equation

$$H = \ln \lambda_1^{EL} \tanh\left(\ln \lambda_1^{EL}\right), \tag{53}$$

for the critical stretch λ_1^{EL} at the ellipticity loss, corresponding to the critical level of shear prestrain γ^{EL}.

When the elliptic boundary is approached, two shear bands are predicted to emerge for a J_2-deformation theory material, inclined at the angles $\pm\theta_0$ with respect to the principal axis x_1

$$\theta_0 = \frac{\pi}{2} - \arctan \lambda_1^{EL}. \tag{54}$$

Finally, it is worth to note that

$$\theta_E \equiv \theta_0 \qquad \text{for} \qquad \lambda_1 > 1, \tag{55}$$

therefore, one shear band direction is perfectly aligned with the inclusion axis, while the other is inclined twice the (anti-clockwise) angle θ_E with respect to inclusion line.

5.1 Validation of the boundary integral formulation

The developed boundary integral method is validated here through a comparison with available analytical solutions referring to two simple cases in which the matrix material is prestressed, but there is only one inclusion, or there are two inclusions, but the matrix material is in an unloaded state.

Published in *Journal of the Mechanics and Physics of Solids* (2022) **165**: 104925
doi: https://doi.org/10.1016/j.jmps.2022.104925

5.1.1 An isolated rigid-line inclusion in a prestressed material

The numerical methodology developed from the presented formulation is compared with the analytical solution obtained in [12] for an isolated rigid-line inclusion (N=1), embedded in an infinite incompressible material, prestressed through a simple shear, and subject to a uniform Mode I perturbation.

The mechanical state near the lamella is characterized in terms of its rigid-body rotation $\Gamma^{(1)} = \omega^{(1)}/\hat{v}^{\infty}_{1,1}$ and of the incremental nominal shear stress jump $[\![\hat{t}_{21}]\!]\,/(\mu\,\hat{v}^{\infty}_{1,1})$ measured across it, as the result of the applied perturbation. These two quantities are reported in Figure 3 for a J_2–deformation theory material with hardening exponent $H = 0.4$, for which ellipticity is lost at an amount of shear $\gamma^{EL} \approx 1.462$, and the shear band inclination is $\theta_0 \approx 0.150\,\pi$.

In the figure, the stress jump $[\![\hat{t}_{21}]\!]$ is reported as a function of the coordinate $\hat{x}_1/l$, for a prestrain $\gamma = 0.992\gamma^{EL} \approx 1.45$. The rigid-body rotation $\Gamma^{(1)}$ is reported as a function of the prestrain $\gamma/\gamma^{EL} \in [-1, 1]$. The numerical solution (dashed line) practically coincides with the analytical one (continuous line), except at the node shared by the two external elements, characterized by different shape functions and representing the transition from the semi-discontinuous to the continuous quadratic element. This reveals that the latter struggles to fit in with the sharp turn due to the square-root singularity at the tip (see the detail at the centre of Figure 3). Although this visible gap delays the solution convergence only at that node, it can be reduced by further decreasing the mesh size there.

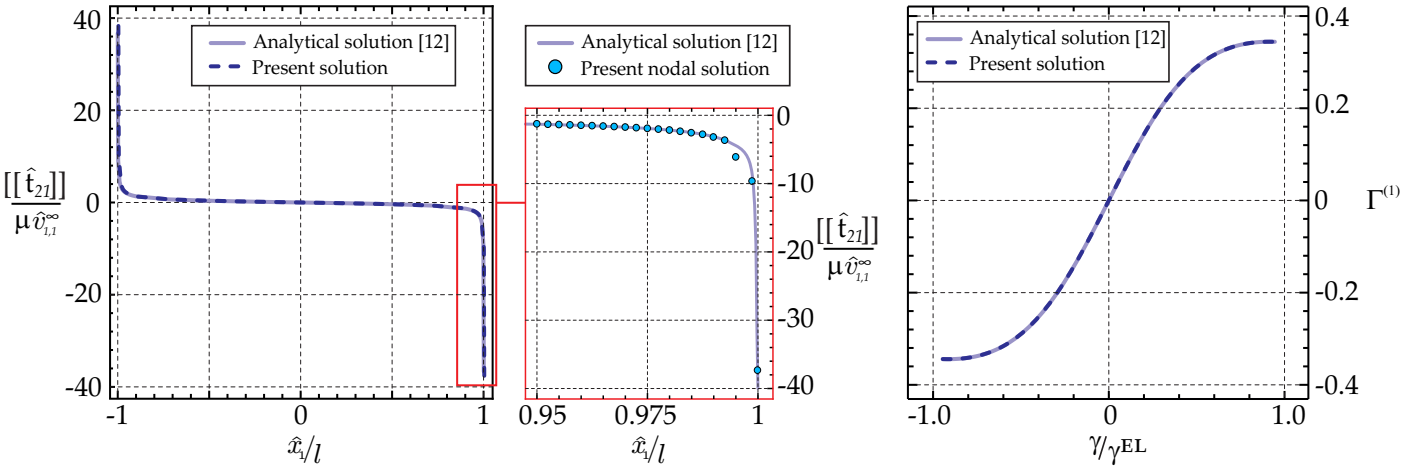

Figure 3: Validation of the proposed numerical methodology in the case when only one rigid-line inclusion is present in an infinite, prestrained matrix (characterized by an incremental shear modulus μ), obeying the J_2–deformation theory of plasticity with $H = 0.4$ and subject to a remote incremental strain $\hat{v}^{\infty}_{1,1}$. Numerical simulations (dashed line) and analytical results (continuous line) are practically coincident, showing the effectiveness of the proposed technique. Left (and detail on the central part): jump in the nominal shear stress $[\![\hat{t}_{21}]\!]$ across the lamella for $\gamma = 1.45 \approx 0.992\gamma^{EL}$ versus the dimensionless lamella coordinate $\hat{x}_1/l$. Right: the rigid-body rotation $\Gamma^{(1)} = \omega^{(1)}/\hat{v}^{\infty}_{1,1}$ displayed by the lamella as a function of the prestrain amount γ.

5.1.2 Two collinear rigid-line inclusions in a linear isotropic incompressible material (at null prestress)

A second validation of the proposed technique is performed through a comparison referring to the case of a linear elastic isotropic incompressible material at null prestress, which can be recovered from the J_2–deformation theory by assuming an hardening exponent equal to the unity, $H = 1$, and a null prestrain, $\gamma = 0$. The presence of two, $N = 2$, collinear rigid-line inclusions of equal length is considered following the scheme presented in Fig. 4, now to be considered only in the case of the undeformed configuration (on the left in the figure). The geometry is specified by

$$C_1^{(2)} = C_1^{(1)} + D, \qquad C_2^{(2)} = C_2^{(1)}, \qquad \Phi = 0, \qquad l^{(1)} = l^{(2)} = l, \tag{56}$$

where $D > 2l$ defines the distance between the inclusion centroids $\mathbf{C}^{(1)}$ and $\mathbf{C}^{(2)}$, the angle Φ is the inclination of the line joining the inclusion centers with respect to the $\hat{X}_1$-axis, and l is the semi-length, equal for both inclusions.

Published in *Journal of the Mechanics and Physics of Solids* (2022) **165**: 104925
doi: https://doi.org/10.1016/j.jmps.2022.104925

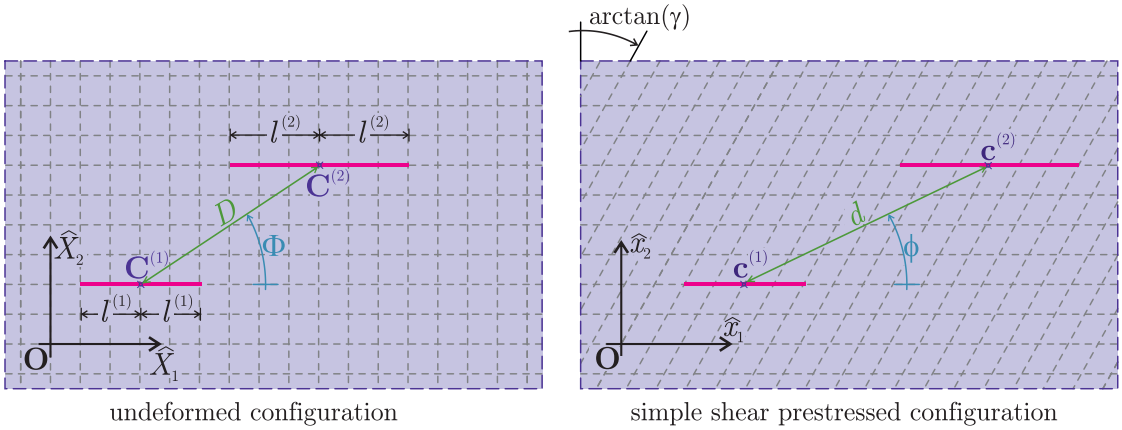

Figure 4: Undeformed (left) and deformed (right) configurations of two parallel rigid-line inclusions embedded in an infinite matrix material subject to a simple shear of amount γ parallel to the horizontal axis. The relative position of two lamellae is described by the distance D between their centroids, points $\mathbf{C}^{(1)}$ and $\mathbf{C}^{(2)}$, and the angle Φ in the undeformed configuration, transformed respectively into d, $\mathbf{c}^{(1)}$, $\mathbf{c}^{(2)}$, and ϕ after deformation.

Due to the symmetry of both geometry and loading, the incremental Mode I SIFs, eqns (15), referred to the four tips, satisfy the following identities

$$\hat{K}^{(2)}_{I,L} = \hat{K}^{(1)}_{I,R} = \hat{K}^{(N=2)}_{I,inn}, \qquad \hat{K}^{(2)}_{I,R} = \hat{K}^{(1)}_{I,L} = \hat{K}^{(N=2)}_{I,out}, \tag{57}$$

where $\hat{K}^{(N=2)}_{I,inn}$ and $\hat{K}^{(N=2)}_{I,out}$ are the incremental SIF at the inner and outer tips respectively, obtained analytically as [41]

$$\left.\begin{matrix}\hat{K}^{(N=2)}_{I,out}\\ \hat{K}^{(N=2)}_{I,inn}\end{matrix}\right\} = \mu\hat{v}^{\infty}_{1,1}\sqrt{\frac{l}{\pi}}\int_{-1}^{1}\left[1+\frac{1}{2-\frac{1}{2}\left(\sqrt{\frac{D}{l}\left(\frac{D}{l}+2\right)}-\sqrt{\frac{D}{l}\left(\frac{D}{l}-2\right)}\right)}\frac{\zeta+\frac{D}{l}}{\sqrt{\left(\zeta+\frac{D}{l}\right)^2-1}}\right]\sqrt{\frac{1\pm\zeta}{1\mp\zeta}}\,\mathrm{d}\zeta. \tag{58}$$

The SIFs $\hat{K}^{(N=2)}_{I,inn}$ and $\hat{K}^{(N=2)}_{I,out}$ are plotted in Figure 5, normalized through division by the corresponding quantity $\hat{K}^{(N=1)}_{I}$ holding for the single inclusion, eqn (16). An excellent agreement is shown between the analytical values (continuous line) from eqn (58) and the numerical evaluation (spots) from the present boundary integral technique.

5.2 Interactions between shear bands and rigid lamellae

The developed formulation is exploited to analyze the incremental mechanical response to a remote Mode I perturbation, uniform at a large distance from the lamellae, when the matrix material (characterized by hardening exponent $H = 0.4$) is prestrained up to a level close to ellipticity loss, $\gamma = 0.992\gamma^{EL}$. Consideration of this prestress state allows for the analysis of shear band formation and interaction. It is recalled that, in the case of an isolated rigid-line inclusion, the shear band direction aligned with the lamella axis is dominant, while the other, developed in the conjugate direction, remains 'weaker' [12, 13]. This pattern is considered in the following as a reference state to disclose the influence on shear bands of various distributions of lamellae. To this purpose, recalling that the incremental strain $\hat{\boldsymbol{\varepsilon}}$ is the symmetric part of the incremental displacement gradient, $\hat{\varepsilon}_{ij} = (\hat{v}_{i,j} + \hat{v}_{j,i})/2$, and it is deviatoric because of incompressibility ($\mathrm{dev}\hat{\boldsymbol{\varepsilon}} = \hat{\boldsymbol{\varepsilon}}$), the results are reported in terms of the modulus of the perturbed incremental strain, $\left|\hat{\boldsymbol{\varepsilon}} - \hat{\boldsymbol{\varepsilon}}^{\infty}\right|$, where the (colored) contours scale is the same for all Figs. 6, 7, 9, and 14 and is such that red corresponds to regions where $\left|\hat{\boldsymbol{\varepsilon}} - \hat{\boldsymbol{\varepsilon}}^{\infty}\right| > 2.6\left|\hat{\boldsymbol{\varepsilon}}^{\infty}\right|$.

Published in *Journal of the Mechanics and Physics of Solids* (2022) **165**: 104925
doi: https://doi.org/10.1016/j.jmps.2022.104925

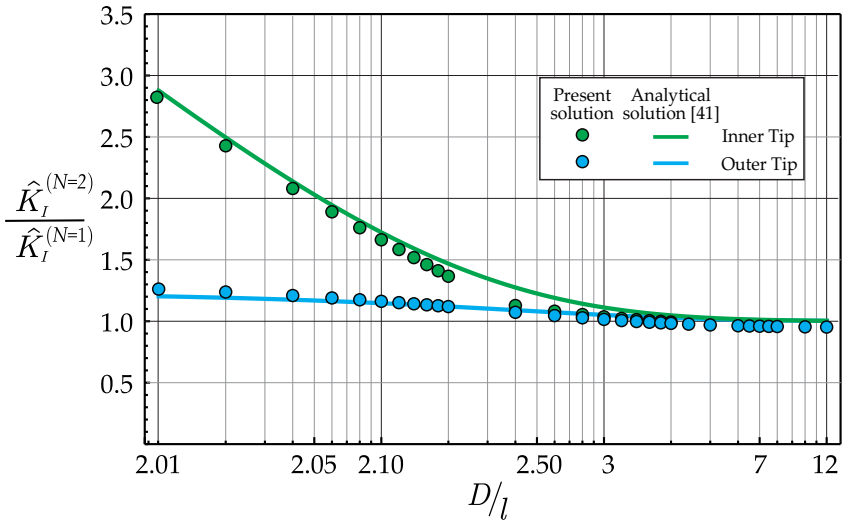

Figure 5: Validation of the proposed numerical methodology in the case of two collinear rigid-line inclusions, embedded in an infinite, unloaded matrix, obeying incompressible, isotropic elasticity. Incremental Stress Intensity Factors $\hat{K}_I^{(N=2)}$ (divided by $\hat{K}_I^{(N=1)} = 2\mu\,\hat{v}_{1,1}^{\infty}\sqrt{\pi l}$) are reported for the outer (blue) and inner (green) tips of two lamellae of length $2l$, as functions of the distance D between their centers. Numerical simulations (spots) are almost superimposed on the available analytical solution (line), eqn (58), showing the effectiveness of the proposed technique.

5.2.1 Prestressed matrix with two rigid-line inclusions

The interaction between two rigid lamellae ($N = 2$), characterized by different length and embedded in a ductile metal matrix is considered, when a Mode I incremental perturbation is applied, superimposed upon a certain prestress induced by a simple shear loading of finite amount. The position of the two rigid inclusions is defined by introducing the following relations between the coordinates of the inclusion centroids in the undeformed configuration (Fig. 4, left)

$$C_1^{(2)} = C_1^{(1)} + D\cos\Phi, \qquad C_2^{(2)} = C_2^{(1)} + D\sin\Phi, \qquad \text{with} \begin{cases} D > 0, & \text{if} \quad \Phi \neq 0, \\ D > l^{(1)} + l^{(2)}, & \text{if} \quad \Phi = 0, \end{cases} \tag{59}$$

where D is the distance between the two centers of the rigid inclusions and Φ is the angle measuring the inclination of the line joining the two centers with respect to the $\hat{x}_1$-axis. Subject to a simple shear deformation, the configuration of the rigid inclusions changes, so that the centroid coordinates c_1, c_2, singling out the deformed configuration, become (Figure 4, right)

$$c_1^{(2)} = c_1^{(1)} + d\cos\phi, \qquad c_2^{(2)} = c_2^{(1)} + d\sin\phi, \tag{60}$$

where d and ϕ are respectively the distance and the inclination, related to the initial values D and Φ through the amount of shear γ as

$$d(D,\Phi,\gamma) = D\sqrt{1 + \gamma\sin 2\Phi + \gamma^2\sin\Phi}, \qquad \phi(\Phi,\gamma) = \arctan\left(\frac{\sin\Phi}{\cos\Phi + \gamma\sin\Phi}\right). \tag{61}$$

Because of the polar symmetry, the fields calculated for the initial angle $\Phi - \pi$ are identical to those calculated for the angle Φ and therefore the investigation is restricted to $\Phi \in [0, \pi)$. Furthermore, elementary geometrical considerations lead to the observation that when $D > l^{(1)} + l^{(2)}$ (when $D < l^{(1)} + l^{(2)}$) the mechanical response is continuous (is discontinuous) at $\Phi = 0$ and $\Phi = \pi$. The above described layout is analyzed in the following for specific geometries, so to dissect the respective influences of the various parameters.

Published in *Journal of the Mechanics and Physics of Solids* (2022) **165**: 104925
doi: https://doi.org/10.1016/j.jmps.2022.104925

Two rigid-line inclusions with centers aligned on the same vertical axis in the undeformed state ($\Phi = \pi/2$). The modulus of the perturbed incremental strain $|\hat{\boldsymbol{\varepsilon}} - \hat{\boldsymbol{\varepsilon}}^{\infty}|$ is reported in Fig. 6 in the surroundings of two rigid-line inclusions. The latter have the inclusion centers aligned vertically in the undeformed state, so that the configuration is described by equation (60) with $\Phi = \pi/2$. The prestrain level is $\gamma \approx 0.992\gamma^{EL}$ and the inclusions are analyzed at varying distance $D = \{0.04, 0.2, 0.5\}l$ (decreasing from the upper to the lower part of the figure). The cases of inclusions with same length ($l^{(1)} = l^{(2)} = l$) and with different length ($l^{(1)} = 2l^{(2)} = l$) are reported on the left and on the right, respectively. Both cases show that, for a prestrain state close to the loss of ellipticity, the deviatoric strain is localized into two principal shear bands parallel to the inclusion lines. These two shear bands, when the two inclusions are sufficiently close, '*merge*' *in one thick shear band*, completely enclosing both inclusions.

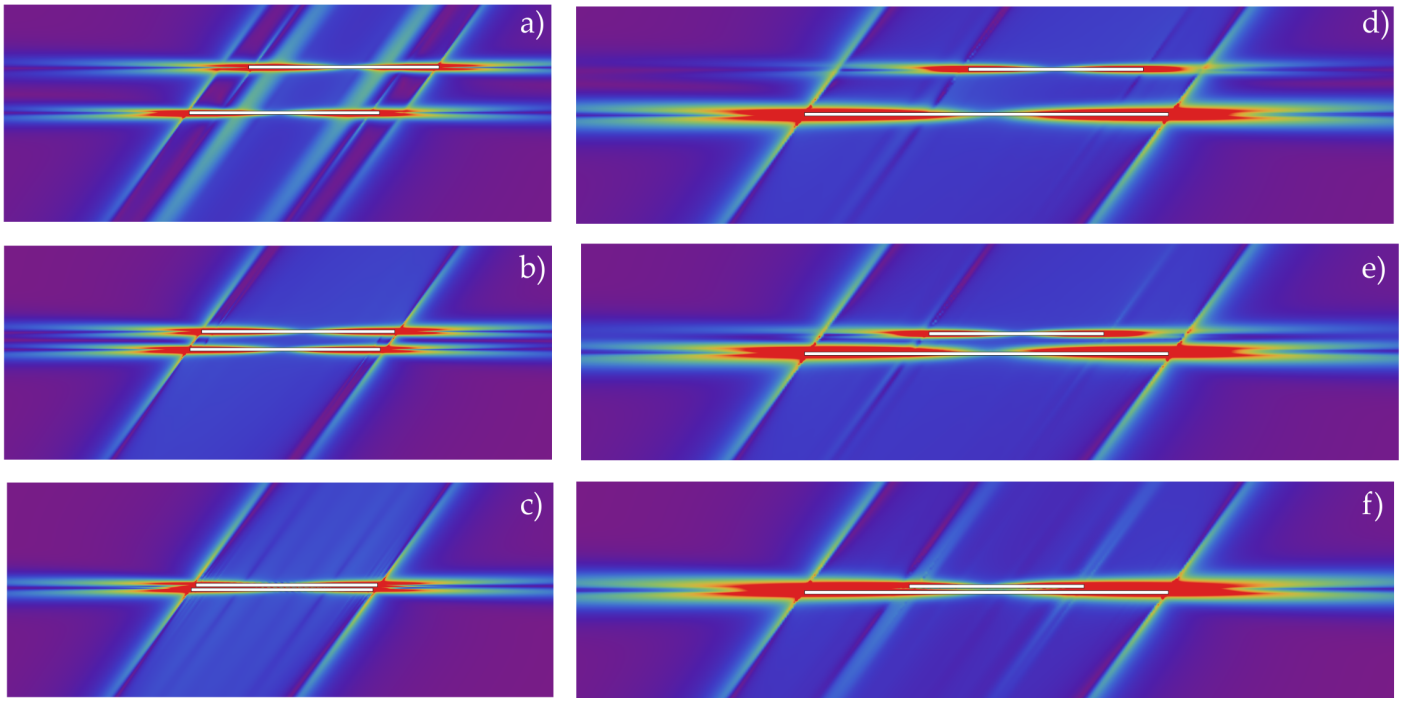

Figure 6: Level sets of the modulus of the perturbed incremental strain $|\hat{\boldsymbol{\varepsilon}} - \hat{\boldsymbol{\varepsilon}}^{\infty}|$ near two lamellae at three different distances $D/l = \{0.04, 0.2, 0.5\}$ (decreasing from the upper to the lower part) and angle $\Phi = \pi/2$, for a simple shear prestrain level $\gamma = 0.992\gamma^{EL}$, after a Mode I remote perturbation. The two lamellae have the same length ($l^{(1)} = l^{(2)} = l$, left column) or one length is twice the other ($l^{(1)} = 2l^{(2)} = l$, right column). Note that when the lamellae are close enough to each other a thick horizontal shear band prevails, involving both rigid-lines.

Two collinear rigid-line inclusions of different length ($\Phi = 0$). Two collinear inclusions with different length, namely, $l^{(1)} = 5l^{(2)} = 5l$, are analyzed at varying distance D. The modulus of the perturbed incremental strain $|\hat{\boldsymbol{\varepsilon}} - \hat{\boldsymbol{\varepsilon}}^{\infty}|$ is reported in Fig. 7 for $D = \{11, 8, 7\}l$ (decreasing from the upper to the lower part). The figure shows that, when the tips of the two inclusions are sufficiently close to each other, the two principal shear bands concur to generate *one very long shear band*, completely enclosing both inclusions.

Two rigid-line inclusions of equal length ($l^{(1)} = l^{(2)} = l$). The case of two inclusions with same length is analyzed at varying reciprocal distance D and angle Φ.

It is interesting to note that the values of inclination Φ and distance D also define the position of one inclusion in relation to the two shear bands inclined at $2\theta_0$ with respect to $\hat{x}_1$ and originating at the tips of the other inclusion in the simple shear deformation state. In particular, three special inclinations, $\widetilde{\Phi}$, $\Phi^{(-)}$, and $\Phi^{(+)}$, can be defined as those

Published in *Journal of the Mechanics and Physics of Solids* (2022) **165**: 104925
doi: https://doi.org/10.1016/j.jmps.2022.104925

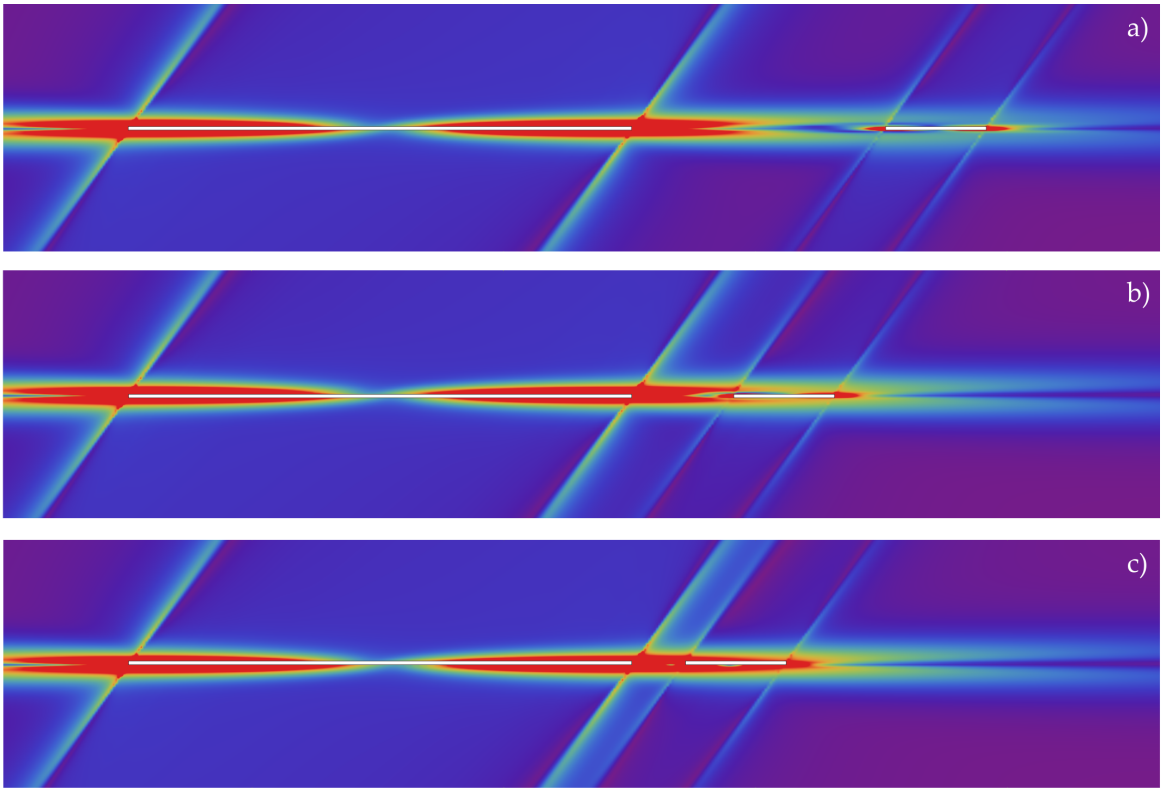

Figure 7: Level sets of the modulus of the perturbed incremental strain $\left|\hat{\boldsymbol{\varepsilon}} - \hat{\boldsymbol{\varepsilon}}^{\infty}\right|$ near two collinear ($\Phi = 0$) lamellae of length $l^{(1)} = 5l^{(2)} = 5l$ at three different distances $D/l = \{7, 8, 11\}$ (decreasing from above to bottom), for a simple shear prestrain level $\gamma = 0.992\gamma^{EL}$, after a Mode I remote perturbation. Note that when the lamellae are close enough to each other a very long shear bands prevails, involving both rigid-lines.

satisfying the relations[2]

$$\widetilde{\Phi} = \arctan\left(-\frac{2}{\gamma^{EL}}\right), \qquad \frac{D}{2l}\left[\cos\Phi^{(\pm)} - \frac{\sin\Phi^{(\pm)}}{\tan\widetilde{\Phi}}\right] = \pm 1, \tag{62}$$

and discriminating the following two interesting cases.

- When $\Phi = \widetilde{\Phi}$, both tips of each inclusion touch the inclined shear bands originated from the tips of the other inclusion. Therefore, each inclusion is enclosed inside the domain defined by the inclined shear bands originated from the tips of the other inclusion;
- When either $\Phi = \Phi^{(+)}(D/2l)$ or $\Phi = \Phi^{(-)}(D/2l)$, only one tip of each inclusion touches the inclined shear band originated from the tip of the other inclusion.

The above-introduced three 'special' inclinations divide the $D/2l - \Phi$ plane into four domains (Fig. 8):

$$\mathcal{E}^{(+)} := \left\{ \{D, \Phi\} \text{ such that } \left|\cos\Phi - \frac{\sin\Phi}{\tan\widetilde{\Phi}}\right| > \frac{2l}{D} \text{ and } 0 < \Phi < \widetilde{\Phi} \right\},$$

$$\mathcal{E}^{(-)} := \left\{ \{D, \Phi\} \text{ such that } \left|\cos\Phi - \frac{\sin\Phi}{\tan\widetilde{\Phi}}\right| > \frac{2l}{D} \text{ and } \widetilde{\Phi} < \Phi < \pi \right\},$$

[2]The identity $\gamma^{EL}\tan 2\theta_0 = 2$ is exploited to obtain eqns (62) together with the following properties

$$\Phi^{(+)} < \widetilde{\Phi} < \Phi^{(-)}, \qquad \widetilde{\Phi} > \pi/2.$$

Published in *Journal of the Mechanics and Physics of Solids* (2022) **165**: 104925
doi: https://doi.org/10.1016/j.jmps.2022.104925

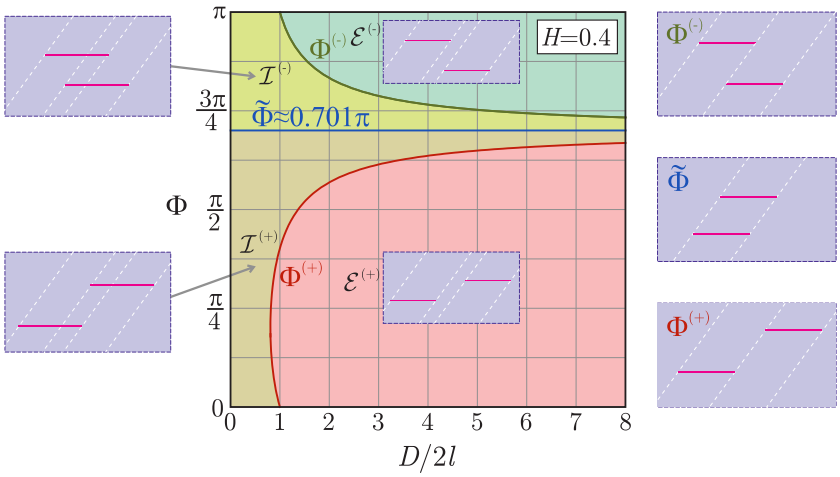

Figure 8: 'Special' inclination angles $\left(\widetilde{\Phi}, \Phi^{(-)}, \Phi^{(+)}\right)$ and domains $\left(\mathcal{E}^{(+)}, \mathcal{E}^{(-)}, \mathcal{I}^{(+)}, \mathcal{I}^{(-)}\right)$ in the $\Phi - D/2l$ plane, distinguishing (in the prestressed configuration) the position of one lamella with respect to the inclined shear band emerging from the tip of the other rigid-line. The plot refers to a J_2-deformation theory material with hardening exponent $H = 0.4$.

$$\mathcal{I}^{(+)} := \left\{ \{D, \Phi\} \text{ such that } \left|\cos\Phi - \frac{\sin\Phi}{\tan\widetilde{\Phi}}\right| < \frac{2l}{D} \text{ and } 0 < \Phi < \widetilde{\Phi} \right\},$$

$$\mathcal{I}^{(-)} := \left\{ \{D, \Phi\} \text{ such that } \left|\cos\Phi - \frac{\sin\Phi}{\tan\widetilde{\Phi}}\right| < \frac{2l}{D} \text{ and } \widetilde{\Phi} < \Phi < \pi \right\},$$

corresponding to prestressed configurations (at the ellipticity loss) where each inclusion lies partially inside ($\mathcal{I}^{(+)}$ and $\mathcal{I}^{(-)}$) or completely outside ($\mathcal{E}^{(+)}$ and $\mathcal{E}^{(-)}$) the strip region defined by the inclined shear bands originated from the tips of the other inclusion.

Due to polar symmetry, the incremental rigid-body rotations of the two inclusions coincide

$$\omega^{(1)} = \omega^{(2)} = \omega^{(N=2)} = \Gamma^{(N=2)} \hat{v}^{\infty}_{1,1}, \tag{63}$$

where $\Gamma^{(N=2)}$ is the dimensionless rotation, and two of the four incremental SIFs at the lamellae tips, eqn (15), are coincident

$$\hat{K}^{(2)}_{I,R} = \hat{K}^{(1)}_{I,L}, \qquad \hat{K}^{(2)}_{I,L} = \hat{K}^{(1)}_{I,R}. \tag{64}$$

The influence of the inclusions' position with respect to the inclined shear bands is highlighted through the map of the modulus of the perturbed incremental strain $\left|\hat{\varepsilon} - \hat{\varepsilon}^{\infty}\right|$ in Fig. 9 and through the sketch of the incrementally deformed configurations in Fig. 10. In particular, the latter figure reports the incremental deformed configurations due to the Mode I perturbation for a mesh of identical squares in the undeformed state. In both figures, the centroids distance is constant, $D = 2l$, while three values for the angle Φ are considered: $\Phi^{(+)} = 0.399\pi$ (left), $\Phi = 0.550\pi \in (\Phi^{(+)}, \widetilde{\Phi})$ (center), and $\widetilde{\Phi} = 0.700\pi$ (right).

For $\Phi = 0.550\pi$ (Figs. 9 and 10, central parts) an inclined shear band, emanating from right tip of the lower rigid-line, intersects the central part of the upper lamella. The intersecting shear band results to be thin, so that *a shear band intersecting a rigid lamella suffers a reduction in 'intensity'*.

An opposite situation is visible for $\Phi^{(+)}$ and $\widetilde{\Phi}$ (Figs. 9 and 10, on the left and right). Here, the tips of the upper and lower lamellae are respectively aligned along one or two inclined shear bands, *resulting in a strong amplification*. More specifically, the case of the alignment of one tip pair ($\Phi^{(+)}$) is substantially different from that of two tip pairs ($\widetilde{\Phi}$). Indeed, the aligned tips have opposite incremental displacement in the former case, becoming concordant in the latter. This implies that the incremental rigid-body rotation $\Gamma^{(N=2)}$ for the geometry $\widetilde{\Phi}$ is much larger than that pertaining to the case characterized by $\Phi^{(+)}$.

Published in *Journal of the Mechanics and Physics of Solids* (2022) **165**: 104925
doi: https://doi.org/10.1016/j.jmps.2022.104925

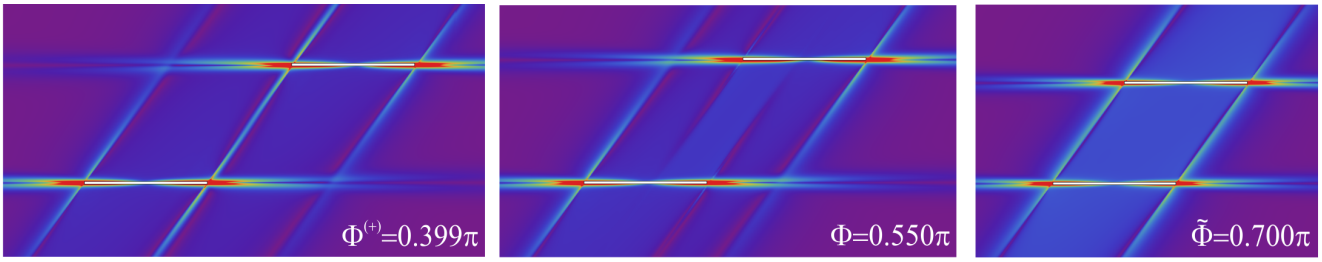

Figure 9: Level sets of the modulus of the perturbed incremental strain $\left|\hat{\boldsymbol{\varepsilon}} - \hat{\boldsymbol{\varepsilon}}^{\infty}\right|$ near two lamellae at a distance $D = 2l$, relative to three different angles $\Phi = \left\{\Phi^{(+)} = 0.399\pi, 0.550\pi, \widetilde{\Phi} = 0.700\pi\right\}$ (from left to right), for a simple shear prestrain level $\gamma = 0.992\gamma^{EL}$, after a Mode I remote perturbation. A strengthening of one or two inclined shear bands is visible in the left or right case, respectively, while a weakening can be observed in the central case.

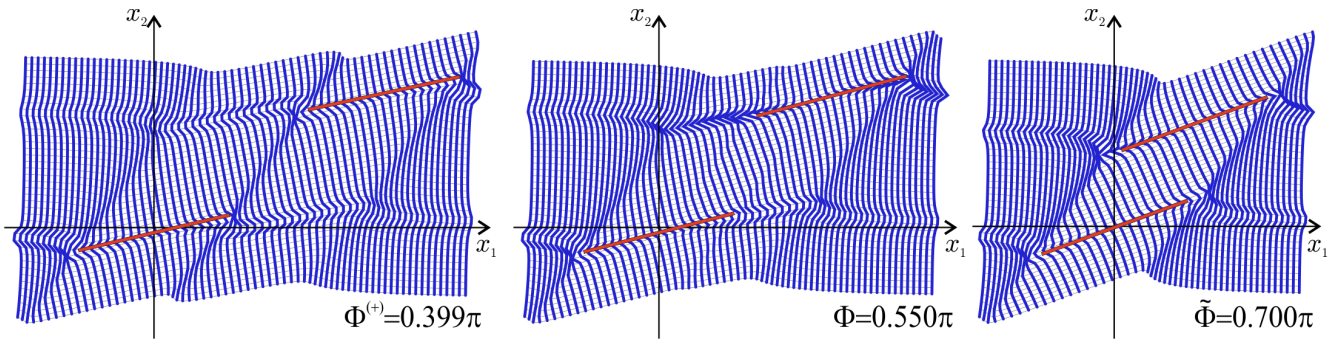

Figure 10: Incremental deformed configurations after Mode I remote perturbation for a mesh of identical squares in the undeformed state. The results shown in this figure correspond to the maps reported in Fig. 9.

To further confirm this behaviour, the incremental rotation $\Gamma^{(N=2)}$ (normalized through division by the corresponding rotation calculated for an isolated lamella, $\Gamma^{(N=1)} = \omega^{(N=1)}/\hat{v}^{\infty}_{1,1}$) is reported in Fig. 11, as a function of the distance D (at fixed angle Φ, left) and of the angle Φ (at fixed distance D, right). The special distributions corresponding to the alignment of one tip pair ($\Phi^{(+)}$ and $\Phi^{(-)}$), or two tip pairs ($\widetilde{\Phi}$), are also reported as dashed curves. In the former case, the rigid-body rotation attains its maximum value, while in the latter the rotation reaches a value close to a relative minimum. Interestingly, when the two lamellae are collinear ($\Phi = 0$), the incremental rotation results unaffected by the distance $D > 2l$ and assumes the same value corresponding to that characteristic of the isolated inclusion, $\Gamma^{(N=2)}(\Phi = 0) = \Gamma^{(N=1)}$.

The above discussion is completed with the analysis of the two incremental SIFs $\hat{K}^{(1)}_{I,L}$ and $\hat{K}^{(1)}_{I,R}$ displayed in Fig. 12 (respectively on the upper and lower part), as functions of the distance D (at a specific angle Φ, left) and of the angle Φ (at a specific distance D, right). These curves are complemented by those reported as dashed curves and corresponding to the special geometries involving the alignment of one tip pair ($\Phi^{(+)}$ and $\Phi^{(-)}$) and of two tip pairs ($\widetilde{\Phi}$). From these curves, it can be observed that $\hat{K}^{(1)}_{I,L}$ ($\hat{K}^{(1)}_{I,R}$) is almost constant and close to the value $\hat{K}^{(N=1)}_{I}$ pertaining to the isolated inclusion, when $\Phi \in (\widetilde{\Phi}, \pi)$ ($\Phi \in (0, \widetilde{\Phi})$). This behaviour is consequent to the fact that the singular field at the relevant tip is unaffected by those belonging to the other lamella, which is shielded by the inclined shear band.

Moreover, $\hat{K}^{(1)}_{I,L}$ and $\hat{K}^{(1)}_{I,R}$ attain a local maximum for the special geometry respectively defined by $\Phi = \Phi^{(+)}$ and $\Phi = \Phi^{(-)}$. This is related to the special alignments between tip pairs, as shown in Fig. 8.

Finally, the incremental SIFs display a strong variation near $\Phi = \widetilde{\Phi}$, because the corresponding geometry is close to the alignment of two tip pairs.

Published in *Journal of the Mechanics and Physics of Solids* (2022) **165**: 104925
doi: https://doi.org/10.1016/j.jmps.2022.104925

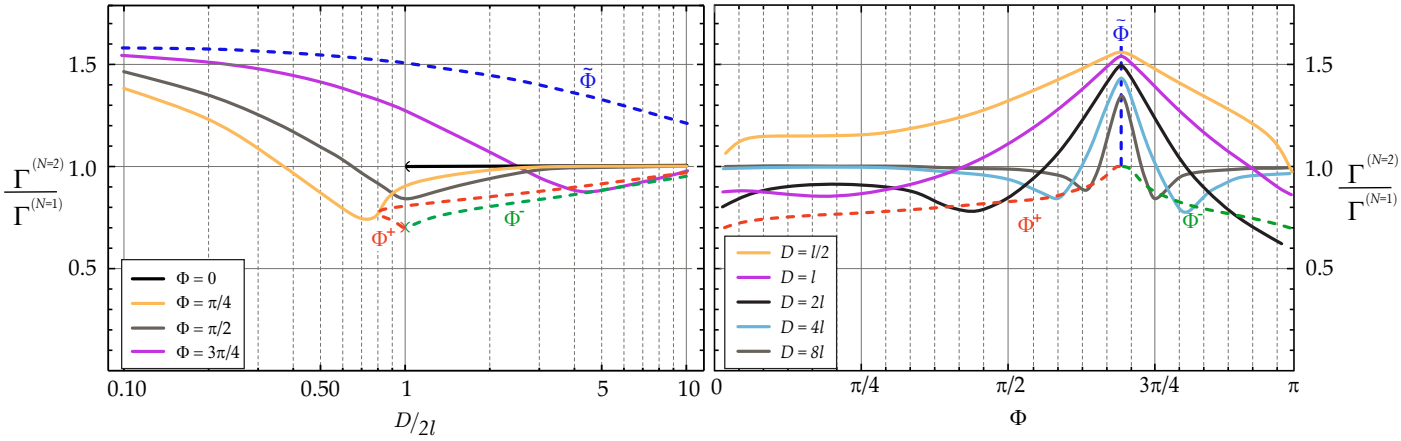

Figure 11: Incremental rigid-body rotation, $\Gamma^{(1)} = \Gamma^{(2)} = \Gamma^{(N=2)}$ (normalized through division by $\Gamma^{(N=1)}$), as a function of the dimensionless distance $D/2l$ for two lamellae of equal length at different angles $\Phi = \{0, 1/4, 1/2, 3/4\}\pi$ (left) and as a function of the angle Φ, at different distances $D/l = \{1/2, 1, 2, 4, 8\}$ (right). Values corresponding to the special geometries of aligned tips are reported as dashed curves, showing that the case $\Phi = \widetilde{\Phi}$ provides the maximum rotation, while the cases $\Phi^{(+)}$ and $\Phi^{(-)}$ correspond to a rotation close to a relative minimum.

5.3 Amplification, reduction, and shielding of shear bands pattern for multiple inclusions

Interactions between lamellae are now investigated for four different polar symmetric distributions of $N = 4$ and $N = 5$ inclusions, as reported in Fig. 13, at the simple shear prestrain level $\gamma = 0.992\gamma^{EL}$. The purpose of the investigation is to cover all the possible different geometric conditions ($\widetilde{\Phi}, \Phi^{(+)}, \Phi^{(-)}, \mathcal{I}^{(+)}, \mathcal{I}^{(-)}, \mathcal{E}^{(+)}, \mathcal{E}^{(-)}$), involving different pairs of inclusions. More specifically, four polar symmetric distributions are analyzed, satisfying the following geometrical conditions in the prestressed state:

Fig. 13a) – four inclusions of length $2l$ are positioned following a scheme of two lines and two inclined columns, where each inclusion has both tips aligned along a line corresponding to the inclined shear bands that develop upon application of the perturbation (geometric conditions $\widetilde{\Phi}$, $\mathcal{E}^{(+)}$, $\mathcal{E}^{(-)}$);

Fig. 13b) – a fifth inclusion of length $2l$ is added in the middle of the distribution a) of lamellae. The central lamella has its tips aligned along the direction of the inclined shear bands emanating, upon application of the perturbation, from the tips of other two inclusions (geometric conditions $\widetilde{\Phi}$, $\Phi^{(+)}$, $\Phi^{(-)}$, $\mathcal{E}^{(+)}$, $\mathcal{E}^{(-)}$);

Fig. 13c) – the five inclusions of distribution b) are shifted in their horizontal position so that the inclusion tips are no longer aligned with respect to the shear band directions (geometric conditions $\mathcal{I}^{(+)}$, $\mathcal{I}^{(-)}$, $\mathcal{E}^{(+)}$, $\mathcal{E}^{(-)}$);

Fig. 13d) – the distribution b) of lamellae is modified by elongating the central inclusion to a length $6l$, so that both tips of this longer lamella are aligned along the two inclined shear bands emanating, upon application of the perturbation, from the outer tips of the other four smaller inclusions (geometric conditions $\widetilde{\Phi}$, $\mathcal{I}^{(+)}$, $\mathcal{I}^{(-)}$, $\mathcal{E}^{(+)}$, $\mathcal{E}^{(-)}$).

Because of polar symmetry, the following identities hold for the incremental rotations and stress intensity factors

$$\Gamma^{(n+2)} = \Gamma^{(n)}, \qquad \hat{K}_{I,R}^{(n+2)} = \hat{K}_{I,L}^{(n)}, \qquad \hat{K}_{I,L}^{(n+2)} = \hat{K}_{I,R}^{(n)}, \qquad \hat{K}_{I,R}^{(5)} = \hat{K}_{I,L}^{(5)}, \qquad n = 1, 2. \tag{65}$$

Maps of the modulus of the perturbed incremental strain $\left|\hat{\boldsymbol{\varepsilon}} - \hat{\boldsymbol{\varepsilon}}^{\infty}\right|$ are reported in Fig. 14 for the four distributions of lamellae shown in Fig. 13, while the corresponding values of incremental rotations $\Gamma^{(n)}$ and incremental stress intensity factors $\hat{K}_{I,L}^{(n)}$ are listed in Table 1, normalized through division by the corresponding quantity calculated for one lamella of length $2l$, $\Gamma^{(N=1)}$ and $\hat{K}_{I}^{(N=1)}$. From the figure and the table it can be concluded that the mechanical response is strongly affected by the inclusion distribution, and in particular:

Published in *Journal of the Mechanics and Physics of Solids* (2022) **165**: 104925
doi: https://doi.org/10.1016/j.jmps.2022.104925

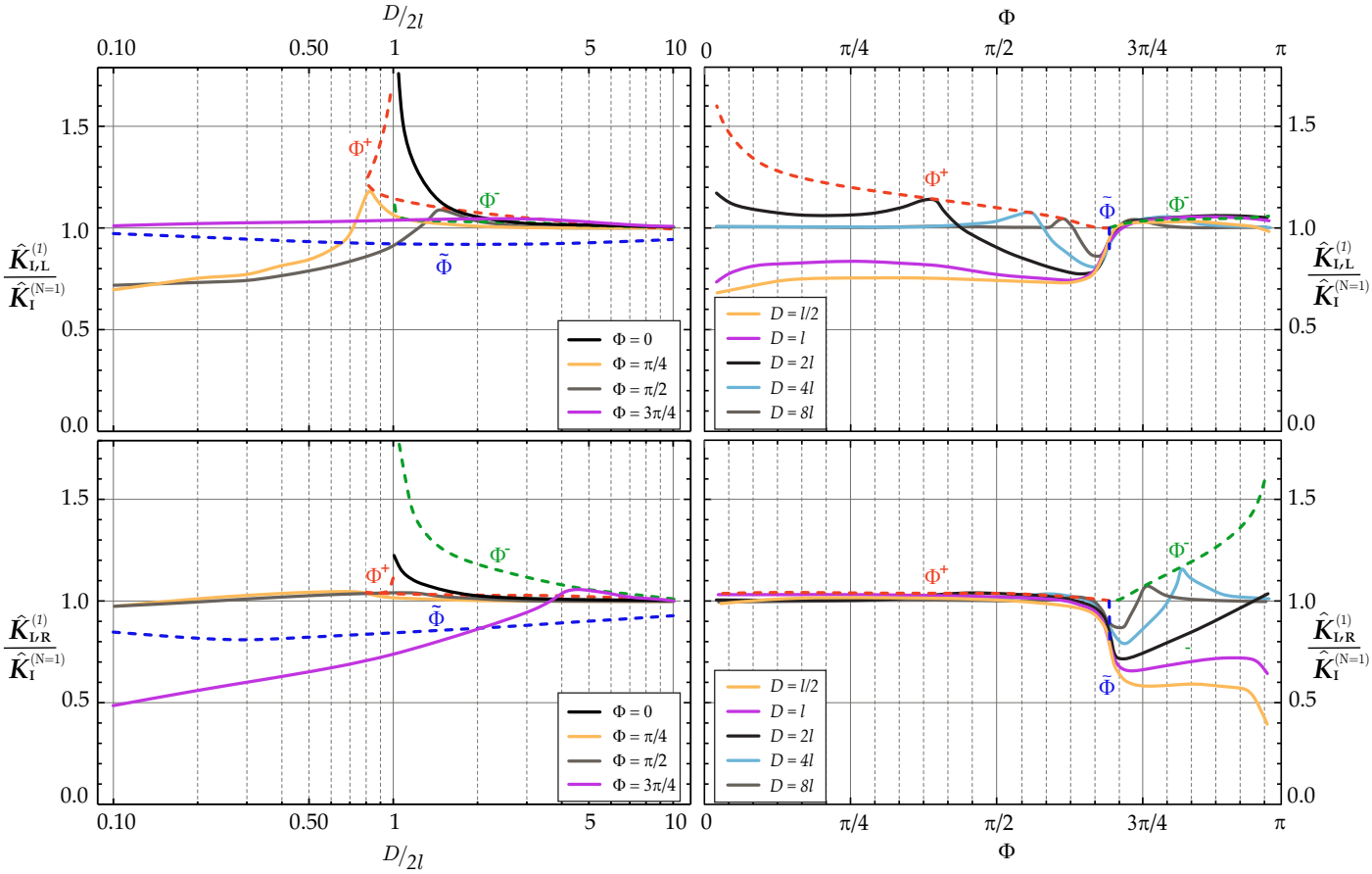

Figure 12: Incremental stress intensity factors $\hat{K}^{(1)}_{I,L}$ (upper part) and $\hat{K}^{(1)}_{I,R}$ (lower part), divided by the value pertaining to one inclusion $\hat{K}^{(N=1)}_{I}$, as functions of the dimensionless distance $D/2l$ (at a specific angle $\Phi = \{0, 1/4, 1/2, 3/4\}\pi$) and of the angle Φ (at a specific distance $D = \{1/2, 1, 2, 4, 8\}l$). Values corresponding to the special geometries of alignment of one tip pair ($\Phi^{(+)}$ and $\Phi^{(-)}$) and of two tip pairs ($\widetilde{\Phi}$) are reported as dashed curves.

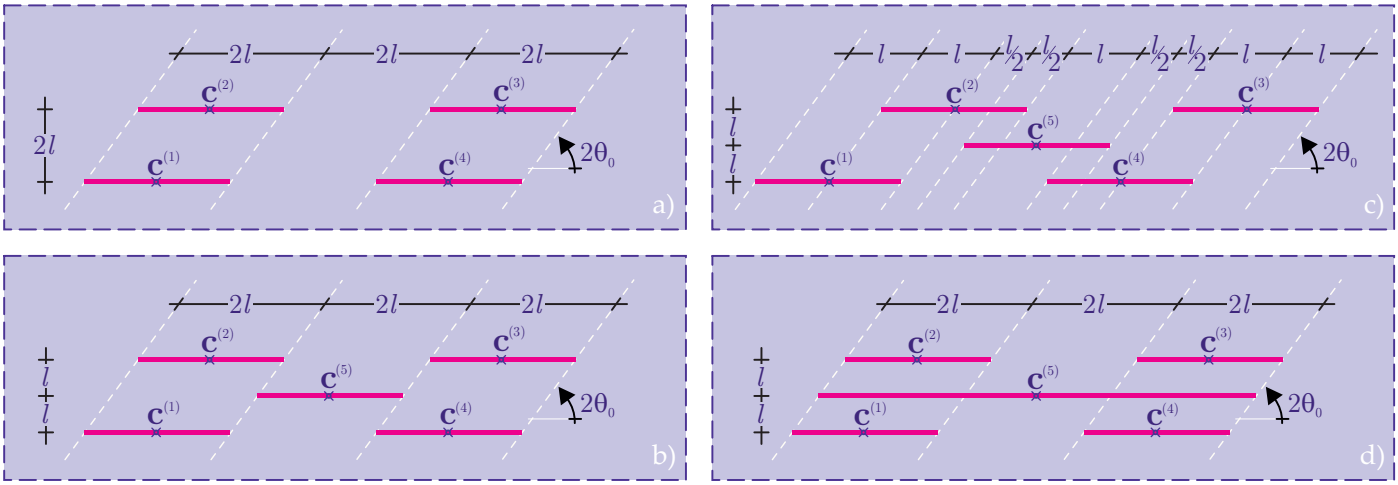

Figure 13: The four considered polar symmetric distributions of thin inclusions ($N = 4$ or $N = 5$) in the deformed configuration after a simple shear of amount $\gamma = 0.992\gamma^{EL}$.

Published in *Journal of the Mechanics and Physics of Solids* (2022) **165**: 104925
doi: https://doi.org/10.1016/j.jmps.2022.104925

	$\frac{\Gamma^{(n)}}{\Gamma^{(N=1)}}$			$\frac{\hat{K}^{(n)}_{I,L}}{\hat{K}^{(N=1)}_{I}}$				
n-th lamella / distribution	1 & 3	2 & 4	5	1	2	3	4	5
a)	1.406	1.403	-	0.920	0.956	0.965	0.920	-
b)	1.185	1.178	0.274	0.989	1.043	1.083	1.092	1.360
c)	1.366	1.365	0.835	0.914	0.952	0.960	0.916	1.051
d)	1.374	1.252	1.426	0.880	1.166	0.794	0.788	1.493

Table 1: Values of incremental rotations $\Gamma^{(n)}$ and incremental stress intensity factors $\hat{K}^{(n)}_{I,L}$ affecting the n-th lamella, for the four lamellae distributions reported in Fig. 13, normalized through division by the corresponding value ($\Gamma^{(N=1)}$ and $\hat{K}^{(N=1)}_{I}$) for the isolated lamella of length $2l$.

- Compared with the shear band patterns developed for distribution a)
  - the inner inclined shear bands are:
    - weakened for distribution b), because of the occurrence of the geometric conditions $\Phi^{(+)}$ and $\Phi^{(-)}$;
    - annihilited for distributions c) and d), because of the occurrence of the geometric conditions $\mathcal{I}^{(+)}$ and $\mathcal{I}^{(-)}$;
  - the outer inclined shear bands are:
    - unchanged for distribution b);
    - weakened for distribution c), because the geometric condition $\widetilde{\Phi}$ does not hold;
    - amplified for distribution d), because of the occurrence of the geometric condition $\Phi^{(+)}$ involving small lamellae and the larger one.

- Compared with the incremental rigid-body rotations occurring for distribution a):
  - the rotations of the non-central lamellae (n=1,2,3,4) of distribution b) are reduced due to the occurrence of geometric condition $\Phi^{(+)}$ or $\Phi^{(-)}$ with the central inclusion (n=5);
  - The rotation of the central lamella (n=5) is approximately equal to the rotation of each of the lateral lamellae (n=1,2,3,4) in distribution d). Moreover, the modulus of the perturbed incremental strain $\left|\hat{\boldsymbol{\varepsilon}} - \hat{\boldsymbol{\varepsilon}}^{\infty}\right|$ is almost constant in the region enclosed by the two outer inclined shear bands. It follows that, roughly speaking, the portion of solid enclosed between the two outer inclined shear bands, and encompassing all the five lamellae, approximately displays an incremental rigid-body rotation.

- With reference to the incremental stress intensity factors:
  - according to the case of two equal inclusions, for the geometric condition $\widetilde{\Phi}$ (Fig. 12, left), the values of $\hat{K}^{(n)}_{I,L}$ for distribution a) are a bit smaller than $\hat{K}^{(N=1)}_{I}$;
  - similarly to the case of two equal inclusions, for the geometric condition $\Phi^{(+)}$ (Fig. 12, left), the value of $\hat{K}^{(5)}_{I,L}$ for distribution b) is greater than $\hat{K}^{(N=1)}_{I}$;
  - because the stress intensity factor is proportional to the square root of the lamella's length, eqn (16), $\hat{K}^{(5)}_{I,L}$ (referred to a lamella of length $6l$) for distribution d) is greater than $\hat{K}^{(N=1)}_{I}$ (referred to a lamella of length $2l$).

Published in *Journal of the Mechanics and Physics of Solids* (2022) **165**: 104925
doi: https://doi.org/10.1016/j.jmps.2022.104925

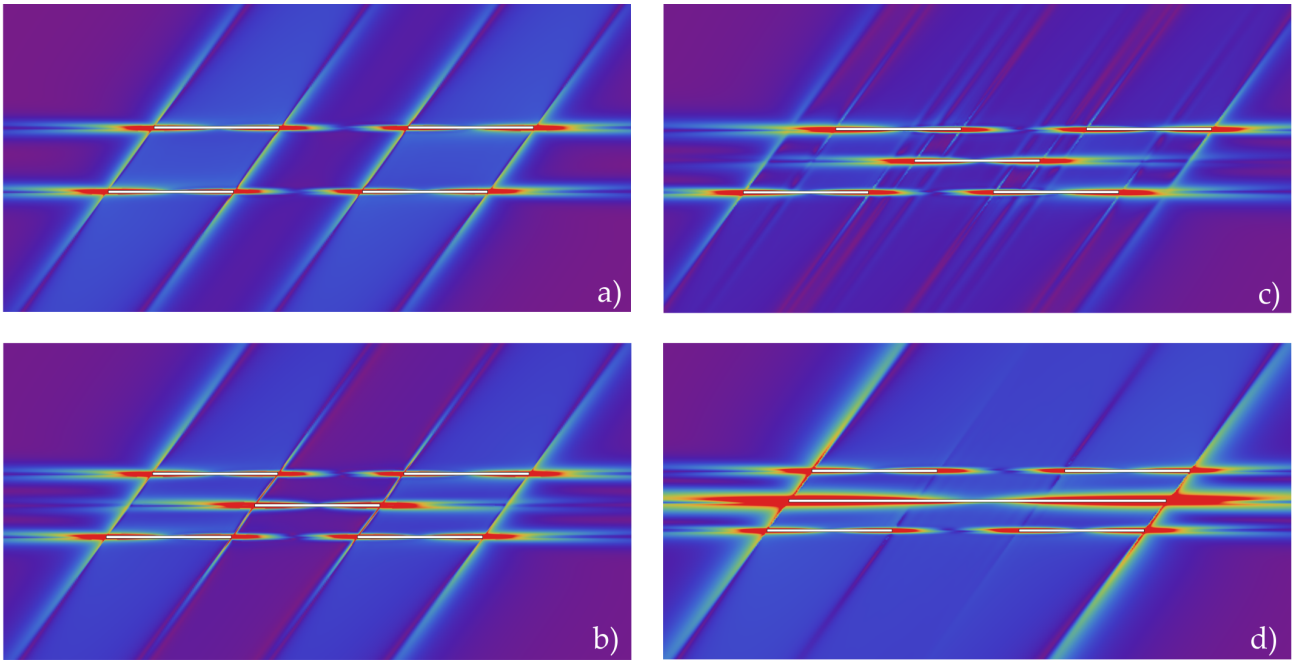

Figure 14: Level sets of the modulus of the perturbed incremental strain $\left|\hat{\boldsymbol{\varepsilon}} - \hat{\boldsymbol{\varepsilon}}^{\infty}\right|$ near the four distributions of lamellae reported in Fig. 13, at a shear prestrain amount $\gamma = 0.992\gamma^{EL}$, close to the boundary of ellipticity loss.

6 Conclusions

A specifically-derived boundary integral equation has been shown to provide a highly detailed description of the incremental strain fields near complex distributions of rigid-line inclusions, embedded in a matrix material. The latter is modelled according to the J_2–deformation theory of plasticity and is subject to a simple shear of finite amount, before the application of a Mode I perturbation. The amount of shear can be high enough to bring the matrix material near failure of ellipticity, where the nucleation and growth of shear bands can be analyzed. This analysis reveals a series of new features related to the failure of a ductile material through shear bands, in particular, mechanisms of weakening or strengthening of shear bands caused by their interactions with the lamellae.

Although developed under quasi-static conditions, the present approach is more general than it might appear. Indeed, it can be extended to analyse the dynamic interaction between multiple lamellae and also to three-dimensional distributions [1, 43, 44], exploiting the Green's function provided by Argani et al. [2].

Acknowledgments. DB and DG acknowledge financial support from the ERC-ADG-2021-101052956-Beyond. FDC gratefully acknowledges financial support from the European Union's Horizon2020 research and innovation programme under the Marie Sklodowska-Curie grant agreement 'LIGHTEN - Ultralight membrane structures towards a sustainable environment' H2020-MSCA-ITN-2020-LIGHTEN-956547. DC acknowledges financial support from FAR - University of Ferrara. Funding from the Italian Ministry of Education, University and Research (MIUR) in the frame of the "Departments of Excellence" grant L. 232/2016 is also acknowledged.

A Linear system for the evaluation of nodal stress jumps and rigid-body parameters

In order to provide the explicit expression for the linear system given by equations (39) and (40), it is instrumental to introduce the numbering of the nodes belonging to each inclusion, so that the p-th inclusion node along the n-th inclusion is defined by coordinates $\left\{ \hat{x}_1^{(n)[p]}, \boldsymbol{C}_2^{(n)} \right\}$ ($p = 1, ..., P^{(n)}$, being $P^{(n)}$ the number of nodes of the n-th inclusion). Defining

P as the total number of nodes,

$$P = \sum_{n=1}^{N} P^{(n)}, \tag{A.1}$$

the linear system, with rank $2P+3N$, can be written as

$$\left[\begin{array}{c|c} \mathcal{U} & \mathcal{A} \\ \hline \mathcal{B} & \mathbf{0} \end{array}\right] \left[\begin{array}{c} \mathbf{T} \\ \hline \mathbf{W} \end{array}\right] = \left[\begin{array}{c} \mathbf{V}^{\infty} \\ \hline \mathbf{0} \end{array}\right], \tag{A.2}$$

where vectors $\mathbf{T}$ and $\mathbf{W}$

$$\mathbf{T} = \left[\mathbf{T}^{(1)}, \dots, \mathbf{T}^{(n)}, \dots, \mathbf{T}^{(N)}\right]^T, \qquad \mathbf{W} = \left[\mathbf{W}^{(1)}, \dots, \mathbf{W}^{(n)}, \dots, \mathbf{W}^{(N)}\right]^T, \tag{A.3}$$

gather vectors $\mathbf{T}^{(n)}$ and $\mathbf{W}^{(n)}$, respectively defined as the collection of the $2P^{(n)}$ nodal incremental stress jumps and the 3 rigid-body incremental displacements of the n-th inclusion ($n = 1, ..., N$)

$$\begin{aligned} \mathbf{T}^{(n)} &= \left[[\![\hat{t}_{21}]\!]^{(n)[1]}, \dots, [\![\hat{t}_{21}]\!]^{(n)[p]}, \dots, [\![\hat{t}_{21}]\!]^{(n)[P^{(n)}]}, [\![\hat{t}_{22}]\!]^{(n)[1]}, \dots, [\![\hat{t}_{22}]\!]^{(n)[p]}, \dots, [\![\hat{t}_{22}]\!]^{(n)[P^{(n)}]} \right], \\ \mathbf{W}^{(n)} &= \left[\eta_1^{(n)}, \eta_2^{(n)}, \omega^{(n)} \right], \end{aligned} \tag{A.4}$$

where $[\![\hat{t}_{2h}]\!]^{(n)[p]}$ is the nodal stress jump across the lamella at node p of the n-th inclusion ($h = 1, 2$). Moreover, vector

$$\mathbf{V}^{\infty} = \left[\mathbf{V}^{\infty(1)}, \dots, \mathbf{V}^{\infty(n)}, \dots, \mathbf{V}^{\infty(N)}\right]^T, \tag{A.5}$$

collects vectors $\mathbf{V}^{\infty(n)}$ defined as ($n = 1, ..., N$)

$$\mathbf{V}^{\infty(n)} = \left[\hat{v}^{\infty}_{1,1}\, \hat{x}_1^{(n)[1]}, \dots, \hat{v}^{\infty}_{1,1}\, \hat{x}_1^{(n)[p]}, \dots, \hat{v}^{\infty}_{1,1}\, \hat{x}_1^{(n)[P^{(n)}]}, C_2^{(n)} \hat{v}^{\infty}_{2,2}, \dots, C_2^{(n)} \hat{v}^{\infty}_{2,2}, \dots, C_2^{(n)} \hat{v}^{\infty}_{2,2} \right]. \tag{A.6}$$

Finally, the coefficient matrices $\mathcal{U}$, $\mathcal{A}$, and $\mathcal{B}$ in equation (A.2) are given by

$$\mathcal{U} = \begin{bmatrix} \mathcal{U}^{(1)(1)} & \mathcal{U}^{(1)(2)} & \dots & \mathcal{U}^{(1)(N)} \\ \mathcal{U}^{(2)(1)} & \mathcal{U}^{(2)(3)} & \dots & \mathcal{U}^{(2)(N)} \\ \vdots & \vdots & \ddots & \vdots \\ \mathcal{U}^{(N)(1)} & \mathcal{U}^{(N)(2)} & \dots & \mathcal{U}^{(N)(N)} \end{bmatrix}, \qquad \mathcal{A} = \begin{bmatrix} \mathcal{A}^{(1)} & 0 & \dots & 0 \\ 0 & \mathcal{A}^{(2)} & \dots & 0 \\ \vdots & \vdots & \ddots & \vdots \\ 0 & 0 & \dots & \mathcal{A}^{(N)} \end{bmatrix}, \qquad \mathcal{B} = \begin{bmatrix} \mathcal{B}^{(1)} & 0 & \dots & 0 \\ 0 & \mathcal{B}^{(2)} & \dots & 0 \\ \vdots & \vdots & \ddots & \vdots \\ 0 & 0 & \dots & \mathcal{B}^{(N)} \end{bmatrix}, \tag{A.7}$$

with ($p = 1, ..., P^{(n)}$; $q = 1, ..., P^{(m)}$)

$$\mathcal{U}^{(m)(n)} = \begin{bmatrix} \mathcal{U}_{11}^{(m)(n)} & \mathcal{U}_{12}^{(m)(n)} \\ \mathcal{U}_{21}^{(m)(n)} & \mathcal{U}_{22}^{(m)(n)} \end{bmatrix}, \qquad \mathcal{U}_{lh}^{(m)(n)} = \begin{bmatrix} u_{lh}^{(m)(n)[1][1]} & \dots & u_{lh}^{(m)(n)[1][p]} & \dots & u_{lh}^{(m)(n)[1][P^{(n)}]} \\ \vdots & \ddots & \vdots & \ddots & \vdots \\ u_{lh}^{(m)(n)[q][1]} & \dots & u_{lh}^{(m)(n)[q][p]} & \dots & u_{lh}^{(m)(n)[q][P^{(n)}]} \\ \vdots & \ddots & \vdots & \ddots & \vdots \\ u_{lh}^{(m)(n)[P^{(m)}][1]} & \dots & u_{lh}^{(m)(n)[P^{(m)}][p]} & \dots & u_{lh}^{(m)(n)[P^{(m)}][P^{(n)}]} \end{bmatrix},$$

$$\mathcal{A}^{(n)} = \begin{bmatrix} 1 & 0 & 0 \\ \vdots & \vdots & \vdots \\ 1 & 0 & 0 \\ 0 & 1 & a^{(n)[1]} \\ \vdots & \vdots & \vdots \\ 0 & 1 & a^{(n)[P^{(n)}]} \end{bmatrix}, \quad a^{(n)[p]} = \hat{x}_1^{(n)[p]} - C_1^{(n)} - \gamma C_2^{(n)}, \quad \mathcal{B}^{(n)} = \begin{bmatrix} b_1^{(n)[1]} & \dots & b_1^{(n)[P^{(n)}]} & 0 & \dots & 0 \\ 0 & \dots & 0 & b_1^{(n)[1]} & \dots & b_1^{(n)[P^{(n)}]} \\ 0 & \dots & 0 & b_2^{(n)[1]} & \dots & b_2^{(n)[P^{(n)}]} \end{bmatrix}, \tag{A.8}$$

where explicit expressions for the coefficients $u_{lh}^{(m)(n)[q][p]}$ and $b_l^{(n)[p]}$ $(l,h=1,2)$ can be specified only once the collocation node positions are defined, with the source node q located along the m-th inclusion and the field node p along the n-th inclusion.

Having assumed the positioning of the collocation points as given by eqn (42), the number of nodes for each inclusion becomes

$$P^{(n)} = 2E^{(n)} + 1, \tag{A.9}$$

and the position of, or the stress jump at, the j-th node $(j=1,2,3)$ of the e-th element $(e=1,...,E^{(n)}-1)$ can be related to that at the p-th node $(p=1,...,P^{(n)})$ as

$$\begin{aligned} \hat{x}_1^{(n)[p]} &= \hat{x}_1^{(n)[2(e-1)+j]} = \hat{x}_1^{(n)(e)(j)}, \\ \left[\!\left[\hat{t}_{2h}\right]\!\right]^{(n)[2(e-1)+j]} &= \left[\!\left[\hat{t}_{2h}\right]\!\right]^{(n)(e)(j)}, \end{aligned} \qquad n=1,...,N. \tag{A.10}$$

Coefficients $u_{lh}^{(m)(n)[q][p]}$ and $b_l^{(n)[p]}$ follow for the first node $(p=1)$ as

$$\begin{aligned} u_{lh}^{(m)(n)[q][1]} &= Q_{kh}Q_{gl}\Delta_1^{(n)}\int_0^1 \varphi_1^{(n)(1)}(\xi)\; v_k^g\left(\mathbf{Q}^T\left(\hat{x}_1^{(n)(1)}+\xi\Delta_1^{(n)}-\hat{x}_1^{(m)[q]}, C_2^{(n)}-C_2^{(m)}\right)\right)\mathrm{d}\xi, \\ b_1^{(n)[1]} &= \Delta_1^{(n)}\int_0^1 \varphi_1^{(n)(1)}(\xi)d\xi, \\ b_2^{(n)[1]} &= \Delta_1^{(n)}\int_0^1 \left(\hat{x}_1^{(n)(1)}+\xi\Delta_1^{(n)}-C_1^{(n)}-\gamma C_2^{(n)}\right)\varphi_1^{(n)(1)}(\xi)d\xi, \end{aligned} \tag{A.11}$$

for the last node $(p=P^{(n)})$ as

$$\begin{aligned} u_{lh}^{(m)(n)[q][P^{(n)}]} &= Q_{kh}Q_{gl}\Delta_{E^{(n)}}^{(n)}\int_0^1 \varphi_3^{(n)(E^{(n)})}(\xi)\; v_k^g\left(\mathbf{Q}^T\left(\hat{x}_1^{(n)(E^{(n)})}+\xi\Delta_{E^{(n)}}^{(n)}-\hat{x}_1^{(m)[q]}, C_2^{(n)}-C_2^{(m)}\right)\right)\mathrm{d}\xi, \\ b_1^{(n)[P^{(n)}]} &= \Delta_{E^{(n)}}^{(n)}\int_0^1 \varphi_3^{(n)(E^{(n)})}(\xi)d\xi, \\ b_2^{(n)[P^{(n)}]} &= \Delta_{E^{(n)}}^{(n)}\int_0^1 \left(\hat{x}_1^{(n)(E^{(n)})}+\xi\Delta_{E^{(n)}}^{(n)}-C_1^{(n)}-\gamma C_2^{(n)}\right)\varphi_3^{(n)(E^{(n)})}(\xi)d\xi, \end{aligned} \tag{A.12}$$

while for the inner non-shared nodes $(p=2,4,6,...,P^{(n)}-3,P^{(n)}-1)$ as

$$\begin{aligned} u_{lh}^{(m)(n)[q][p]} &= Q_{kh}Q_{gl}\Delta_{\frac{p}{2}}^{(n)}\int_0^1 \varphi_2^{(n)\left(\frac{p}{2}\right)}(\xi)\; v_k^g\left(\mathbf{Q}^T\left(\hat{x}_1^{(n)\left(\frac{p}{2}\right)}+\xi\Delta_{\frac{p}{2}}^{(n)}-\hat{x}_1^{(m)[q]}, C_2^{(n)}-C_2^{(m)}\right)\right)\mathrm{d}\xi, \\ b_1^{(n)[p]} &= \Delta_{\frac{p}{2}}^{(n)}\int_0^1 \varphi_2^{(n)\left(\frac{p}{2}\right)}(\xi)d\xi, \\ b_2^{(n)[p]} &= \Delta_{\frac{p}{2}}^{(n)}\int_0^1 \left(\hat{x}_1^{(n)\left(\frac{p}{2}\right)}+\xi\Delta_{\frac{p}{2}}^{(n)}-C_1^{(n)}-\gamma C_2^{(n)}\right)\varphi_2^{(n)\left(\frac{p}{2}\right)}(\xi)d\xi, \end{aligned} \tag{A.13}$$

and, finally, for the inner shared nodes ($p = 3, 5, 7, ..., \boldsymbol{P}^{(n)} - 4, \boldsymbol{P}^{(n)} - 2$) as

$$
\begin{aligned}
u_{lh}^{(m)(n)[q][p]} = \; & Q_{kh} Q_{gl} \left[\Delta^{(n)}_{\frac{p-1}{2}} \int_0^1 \varphi_3^{(n)\left(\frac{p-1}{2}\right)}(\xi)\; v_k^g \left(\mathbf{Q}^T \left(\hat{x}_1^{(n)\left(\frac{p-1}{2}\right)} + \xi \Delta^{(n)}_{\frac{p-1}{2}} - \hat{x}_1^{(m)[q]}, C_2^{(n)} - C_2^{(m)} \right) \right) \mathrm{d}\xi \right. \\
& \left. + \Delta^{(n)}_{\frac{p+1}{2}} \int_0^1 \varphi_1^{(n)\left(\frac{p+1}{2}\right)}(\xi)\; v_k^g \left(\mathbf{Q}^T \left(\hat{x}_1^{(n)\left(\frac{p+1}{2}\right)} + \xi \Delta^{(n)}_{\frac{p+1}{2}} - \hat{x}_1^{(m)[q]}, C_2^{(n)} - C_2^{(m)} \right) \right) \mathrm{d}\xi \right], \\
b_1^{(n)[p]} = \; & \Delta^{(n)}_{\frac{p-1}{2}} \int_0^1 \varphi_3^{(n)\left(\frac{p-1}{2}\right)}(\xi) d\xi + \Delta^{(n)}_{\frac{p+1}{2}} \int_0^1 \varphi_1^{(n)\left(\frac{p+1}{2}\right)}(\xi) d\xi, \qquad \text{(A.14)} \\
b_2^{(n)[p]} = \; & \Delta^{(n)}_{\frac{p-1}{2}} \int_0^1 \left(\hat{x}_1^{(n)\left(\frac{p-1}{2}\right)} + \xi \Delta^{(n)}_{\frac{p-1}{2}} - C_1^{(n)} - \gamma C_2^{(n)} \right) \varphi_3^{(n)\left(\frac{p-1}{2}\right)}(\xi) d\xi \\
& + \Delta^{(n)}_{\frac{p+1}{2}} \int_0^1 \left(\hat{x}_1^{(n)\left(\frac{p+1}{2}\right)} + \xi \Delta^{(n)}_{\frac{p+1}{2}} - C_1^{(n)} - \gamma C_2^{(n)} \right) \varphi_1^{(n)\left(\frac{p+1}{2}\right)}(\xi) d\xi.
\end{aligned}
$$

References

[1] Antonio, J., Tadeu, A., Godinho, L. 2.5D scattering of waves by rigid inclusions buried under a fluid channel via BEM. Eur. J. Mech. - A/Sol. 24, 957–973 (2005).

[2] Argani, L.P., Bigoni, D., Capuani, D., Movchan, N.V. Cones of localized shear strain in incompressible elasticity with prestress: Green's function and integral representations. Proc. R. Soc. A 470:20140423 (2014).

[3] Baranova, S., Mogilevskaya, S.G., Mantic, V., Jimenez-Alfaro, S. Analysis of the Antiplane Problem with an Embedded Zero Thickness Layer Described by the Gurtin-Murdoch Model. J. Elas. 140(2), 171–195 (2020).

[4] Bigoni, D. (2012) Nonlinear Solid Mechanics Bifurcation Theory and Material Instability. Cambridge University Press.

[5] Bigoni, D., Capuani, D. Green's function for incremental nonlinear elasticity: shear bands and boundary integral formulation. J. Mech. Phys. Sol. 50, 471–500 (2002).

[6] Bigoni, D., Dal Corso, F. and Gei, M. The stress concentration near a rigid line inclusion in a prestressed, elastic material. Part II. Implications on shear band nucleation, growth and energy release rate. J. Mech. Phys. Sol. 56, 839–857 (2008).

[7] Bigoni, D., Capuani, D., Bonetti, P., Colli, S. A novel boundary element approach to time-harmonic dynamics of incremental nonlinear elasticity: The role of pre-stress on structural vibrations and dynamic shear banding. Comp. Meth. Appl. Mech. Eng. 196, 4222–4249 (2007).

[8] Bonnet, M. (1999) Boundary Integral Equation Methods for Solids and Fluids. Wiley, Chichester.

[9] Chirino, F. Abascal, R. Dynamic and static analysis of cracks using the hypersingular formulation of the boundary element method. Int. J. Num. Meth. Eng. 43, 365–388 (1998).

[10] Dong, C.Y. The integral equation formulations of an infinite elastic medium containing inclusions, cracks and rigid lines. Eng. Fract. Mech. 75, 3952–3965 (2008).

[11] Dal Corso, F., Bigoni, D. and Gei, M. The stress concentration near a rigid line inclusion in a prestressed, elastic material. Part I. Full field solution and asymptotics. J. Mech. Phys. Sol. 56, 815–838 (2008).

[12] Dal Corso, F., Bigoni, D. The interactions between shear bands and rigid lamellar inclusions in a ductile metal matrix. Proc. R. Soc. A, 465, 143-163 (2009).

[13] Dal Corso, F., Bigoni, D. Growth of slip surfaces and line inclusions along shear bands in a softening material. Int. J. Frac. 166, 225–237 (2010).

[14] Dong, C.Y. Shape optimizations of inhomogeneities of two dimensional (2D) and three dimensional (3D) steady state heat conduction problems by the boundary element method. Eng. Anal. Bound. Elem. 60, 67–80 (2015).

[15] Dong, C.Y., Lo, S.H. Cheung, Y.K. Stress analysis of inclusion problems of various shapes in an infinite anisotropic elastic medium. Comp. Meth. Appl. Mech. Eng. 192, 683–696 (2003).

[16] Dong, C.Y., Lo, S.H., Cheung, Y.K. Numerical analysis of the inclusion-crack interactions using an integral equation. Comp. Mech. 30, 119–130 (2003).

[17] Du, G., Mao, A., Yu, J., Hou, J., Zhao, N., Han, J., Zhao, Q., Gao, W. Xie, T., Bai, H. Nacre-mimetic composite with intrinsic self-healing and shape-programming capability. Nature Comm. 10, 800 (2019).

[18] Garcia, F., Saez, A., Dominguez, J. Traction boundary elements for cracks in anisotropic solids. Eng. Anal. Bound. Elem. 28, 667–676 (2004).

[19] Giarola, D., Capuani, D., Bigoni, D. The dynamics of a shear band. J. Mech. Phys. Sol. 112, 472-490 (2018).

[20] Giarola, D., Capuani, D., Bigoni, D. Dynamic interaction of multiple shear bands. Sci. Rep. 8, 16033 (2018).

[21] Gorski, R., Fedelinski, P. Analysis of composites with rigid reinforcements by the boundary element method. ECCM15 - 15TH Eur. Conf. Comp. Mat. (2012).

[22] Goudarzi, M., Simone, A. Fiber neutrality in fiber-reinforced composites: Evidence from a computational study. Int. J. Sol. Struct. 156–157, 14–28 (2019).

[23] Goudarzi, M., Dal Corso, F., Bigoni, D., Simone, A. Dispersion of rigid line inclusions as stiffeners and shear band instability triggers. Int. J. Sol. Struct. 210–211, 255–272 (2021).

[24] Hu, K.X., Chandra, A., Huang, Y. On crack, rigid-line fiber, and interface interactions. Mech. Mat. 19, 15–28 (1994).

[25] Hutchinson, J.W., Neale, K.W. Finite strain J_2-deformation theory. In: Carlson, D.E., Shield, R.T. (Eds.), Proceedings of the IUTAM Symposium on Finite Elasticity. Martinus Nijhoff, The Hague, Boston, London, 237–247 (1979).

[26] Jobin, T.M., Ramji, M., Khaderi, S.N. Numerical evaluation of the interaction of rigid line inclusions using strain intensity factors. Int. J. Mech. Sci. 153–154, 10–20 (2019).

[27] Jobin, T.M., Khaderi, S.N., Ramji, M. Experimental evaluation of the strain intensity factor at the inclusion tip using digital photoelasticity. Opt. Las. Eng., 126, 105855 (2020).

[28] Jobin, T.M., Khaderi, S.N., Ramji, M. Experimental evaluation of the strain intensity factor at the rigid line inclusion tip embedded in an epoxy matrix using digital image correlation. Theor. Appl. Frac. Mech. 106, 102425 (2020).

[29] Leite, L.G.S. Venturini, W.S. Accurate modelling of rigid and soft inclusions in 2D elastic solids by the boundary element method. Comp. Struct. 84, 1874–1881 (2006).

[30] Li, Q., Ting, T.G.T. Line Inclusions in Anisotropic Elastic Solids. J. Appl. Mech. 56(3), 556–563 (2016).

[31] Liu, Y.J., Nishimura, N., Otani, Y., Takahashi, T., Chen, X.L., Munakata, H. A Fast Boundary Element Method for the Analysis of Fiber-Reinforced Composites Based on a Rigid-Inclusion Model. J. Appl. Mech. 72, 115 (2005).

[32] Ma, L., Qiu, Y., Zhang, Y., Li, G. General solution for inhomogeneous line inclusion with non-uniform eigenstrain. Arch. Appl. Mech. 89, 1723–1741 (2019).

[33] Martin, P.A., Rizzo, F.J. On boundary integral equations for crack problems. Proc. R. Soc. A 421, 341–355 (1989).

[34] Mishuris, G., Piccolroaz, A., Vellender, A. Boundary integral formulation for cracks at imperfect interfaces. Quart. J. Mech. Appl. Math. 67, 363–387 (2014).

[35] Misseroni, D., Dal Corso, F., Shahzad, S., Bigoni, D. Stress concentration near stiff inclusions: validation of rigid inclusion model and boundary layers by means of photoelasticity. Eng. Fract. Mech., 121–122, 87–97 (2014).

[36] Morini, L., Piccolroaz, A. Boundary integral formulation for interfacial cracks in thermodiffusive bimaterials. Proc. R. Soc. A 471:20150284 (2015).

[37] Noselli, G., Dal Corso, F., Bigoni, D. The stress intensity near a stiffener disclosed by photoelasticity. Int. J. Fract. 166, 91–103 (2010).

[38] Pasternak, I., Ilchuk, N. Sulym, H., Andriichuk, O. Boundary integral equations for anisotropic elasticity of solids containing rigid thread-like inclusions. Mech. Res. Comm. 100, 103402 (2019).

[39] Patil, P., Khaderi, S.N., Ramji, M. Numerical estimation of strain intensity factors at the tip of a rigid line inclusion embedded in a finite matrix. Eng. Fract. Mech. 172, 215–230 (2017).

[40] Paulino, G.H., Gray, L.J. Crack Tip Interpolation, Revisited. SIAM J. Appl. Math., 58, 428-455 (1998).

[41] Pingle, P.S., Gorbatikh, L., Sherwood, J.A. Analysis of multiple rigid-line inclusions for application to bio-materials. Proc. of IMECE2007, ASME Int. Mech. Eng. Cong. Expo., Seattle, Washington, USA, 801–807 (2007).

[42] Portela, A., Aliabadi, M. H. Rooke, D.P. The Dual Boundary Element Method:Effective Implementation for Crack Problems. Int. J. Num. Meth. Eng. 33, 1269–1287 (1992).

[43] Tadeu, A., Anto, J. Use of constant, linear and quadratic boundary elements in 3D wave diffraction analysis. Eng. Anal. Bound. Elem. 24, 131–144 (2000).

[44] Tadeu, A., Mendes, P.A., Antonio, J. The simulation of 3D elastic scattering produced by thin rigid inclusions using the traction boundary element method. Comput. Struct. 84, 2244–2253 (2006).

[45] Salvadori, A., Gray, L.J. Analytical integrations and SIFs computation in 2D fracture mechanics. Comp. Meth. Appl. Mech. Eng. 70, 445–495 (2007).

[46] Withers P.J. Metal matrix composite. In: AccessScience. United Kingdom: McGraw-Hill Education; 2014. DOI: 10.1036/1097-8542.418600

[47] Yin, H.L., Liu S.Q., Zhao L.C., Cui, C.X., Wang, X. Vacuum infiltration molding and mechanical property of short carbon fiber reinforced Ti-based metallic glass matrix composite. J. Materials Proc. Tech. 295, 117151 (2021).